Planetary Penetrators for Sample Return Missions

Chad A. Truitt

A thesis

submitted in partial fulfillment of the

requirements for the degree of

Master of Science

University of Washington

2016

Committee:

Robert M. Winglee

Michael McCarthy

Erika Harnett

Program Authorized to Offer Degree:

Earth and Space Sciences

University of Washington

Abstract

Planetary Penetrators for Sample Return Missions

Chad A. Truitt

Chair of the Supervisory Committee:
Professor Robert M. Winglee
Earth and Space Sciences

Sample return missions offer a greater science yield when compared to missions that only employ in situ experiments or remote sensing observations, since they allow the application of more complicated technological and analytical methodologies in controlled terrestrial laboratories that are both repeatable and can be independently verified. The successful return of extraterrestrial materials over the last four decades has contributed to our understanding of the solar system, but retrieval techniques have largely depended on the use of either soft-landing, or touch-and-go procedures that result in high ΔV requirements, and return yields typically limited to a few grams of surface materials that have experienced varying degrees of alteration from space weathering. Hard-landing methods using planetary penetrators offer an alternative for

sample return that significantly reduce a mission's ΔV, increase sample yields, and allow for the collection of subsurface materials, and lessons can be drawn from previous sample return missions. The following details progress in the design, development, and testing of penetrator/sampler technology capable of surviving subsonic and low supersonic impact velocities (<700 m/s) that would enable the collection of geologic materials using tether technology to return the sample to a passing spacecraft. The testing of energy absorbing material for protecting the sample, as well as the design evolution and field testing of the penetrator are discussed. It is shown through field testing that penetrators at speeds between 300-600 m/s (~Mach 1-2) can penetrate into the ground to depths of 1-2 m with overall structural integrity maintained. Four series of test flights are discussed that demonstrate the arc of the research from penetrator survivability, to successful sample collection and ejection of the sample return container. The potential for metamorphic effects during sampling is discussed along with future work that will assist in defining parameters for selecting appropriate primitive bodies for future sample return missions.

TABLE OF CONTENTS

LIST OF FIGURES

LIST OF TABLES

ACKNOWLEDGEMENTS

Funding for this study was provided by NASA Innovative Advanced Concepts under grants NNX12AR02G and NNX13AR37G. As with all efforts in space exploration, the completion of these studies required considerable help and I would like to thank the staff, faculty, and students of the University of Washington's Department of Earth and Space Sciences who tirelessly assisted in the fabrication, testing, and recovery of the systems. I could not have completed any of this work without you.

DEDICATION

For my loving wife who serves as the rock upon which I stand, and my brilliant daughter who keeps me looking toward the stars. Thank you for your patience and continued support.

Chapter 1. SAMPLE RETURN AND SPACECRAFT

1.1 THE IMPORTANCE OF SAMPLE RETURN MISSIONS

The National Research Council [1] advised that Discovery and New Frontier class missions should play a critical role over the next decade in the study of primitive bodies for an understanding of the basic building blocks that created our world, as well as assessing potential hazards impacting bodies represent to our biosphere. Sample return missions from primitive bodies are excellent candidates for NASA's Discovery and New Frontier Programs given their potential for a high science yield while requiring only a fraction of the investment typical of a Flagship mission, and could supply materials long demanded by the science community for furthering our study of the solar system.

In the last decade, private industry's interest in reaching beyond Earth's gravitational influence has increased, as companies look to primitive bodies as a reservoir to augment limited terrestrial resources. The success of SpaceX's efforts in demonstrating civilian launch capabilities has encouraged investment in other organizations like Planetary Resources, and Deep Space Industries that intend to be among the first to harvest valuable metals from the asteroid belt. Table 1.1 shows a representative summary of important materials on extraterrestrial bodies that will play a critical role both in making these commercial ventures profitable, and in developing an understanding of the availability of supplies for In Situ Resource Utilization (ISRU) for future space exploration [2]. It is important to note the lack of confirmed data concerning asteroids and comets in the table, which represent gaps in our knowledge concerning their composition. Sample return missions from these bodies would help provide a

map to the stars, increasing the efficiency of commercial exploration around the solar system, and assist in

Table 1.1. Representative known and unknown compositions of select extraterrestrial bodies, potential ISRU applications, and basic environmental considerations for visiting spacecraft; TBD = to be determined, PGM = platinum group metals, KREEP = potassium rare earth elements phosphorous [2].

	Resources				
	Moon	**Mars**	**Asteroids**	**Comets**	**Outer Planets**
Regolith	H20 ice, O2, OH, Granular powder, Shielding, Insulation Structural, Manufacturing Feedstock	H20 ice, Rocky with sand, Shielding, Structural, Insulation, Manufacturing Feedstock	Varies – granular powder TBD	H20 ice TBD	TBD
Volatiles	H2O, CO, H2, Hg, H2S, NH3, He3, CH4, Ca, C2H6, CH3OH, C2H4	CO2, O, N2, H2O, Cl, Br, Fl, CO, TBD	H20, TBD	H20, CH4, TBD	H, He, CH4,N2 H2O, CO2, CO, NH4, C2H6 TBD
Minerals	Feldspars Pyroxines Olivines Oxides	Basalt Andecite Hematite Silicates Sulfates Carbonates Pegmatities Oxides, TBD	Silicates Oxides TBD	TBD	Silicates Oxides TBD
Metals	Al, Fe, Ti, Mg, Ca, TBD	Al, Fe, Ti, Mg, Ca, Na, Cu, Zn, Pb, Cr, Ni, Co, PGM, TBD	Fe, Ni, Ti, PGM et.c. TBD	TBD	Fe, TBD
Solar Power	Yes	Yes	Yes	Yes	No
Thermal gradients	Yes	Yes	Yes	Yes	Low
Vacuum	Yes	No: CO2, N2, H20, Ar, O2, CO, Ne, Kr, Xe, O3	Yes	Yes	No - varies
Rare Earth Elements	Yes associated with KREEP	TBD	TBD	TBD	TBD
Water	Limited - Poles	Yes	Yes	Yes	Yes - Abundant

establishing the infrastructure necessary for humanity to push further into space by locating potential materials for ISRU.

Scott Sandford, a team member of the OSIRIS-REx mission speaking at an Exploration Science Forum, highlighted some of the advantages sample return missions have over in-situ and remote sensing methods, including: an increase in the quality of the data produced through the application of technology that was not available during the spacecraft's development; returned samples become research resources for both present and future scientists; sample analysis is not limited by design constraints of the spacecraft. He also spoke to their potential to reduce research limitations that result from poor assumptions saying, "…if you decide to measure *A*, and you go there with your *A* measuring machine… it is possible that the main thing that you will learn… is maybe you should have measured *B,* and now you need new spacecraft and another mission" [3].The impact sample return missions will have on our understanding of the solar system cannot be understated, and given the high science yield, relatively low development cost, and long term benefits offered by analysis conducted in controlled terrestrial labs, these missions should have the highest priority in the years to come.

1.2 Sample Return Methods

The earliest evidence of the composition of other solid bodies arrived on Earth in the form of meteorites. Humans have been witness to meteorite falls and collecting their remnants for thousands of years, but only in more recent history has geochemistry began to unlock their compositional secrets. Stark differences in elemental ratios between the Earth and sampled meteorites, as well as between different meteorites themselves, have raised many questions concerning the early formation of solid bodies. Figure 1.1 demonstrates differences in

magnesium and aluminum abundances found in various terrestrial and extraterrestrial samples, along with compositional observations of the Sun's photosphere [4].

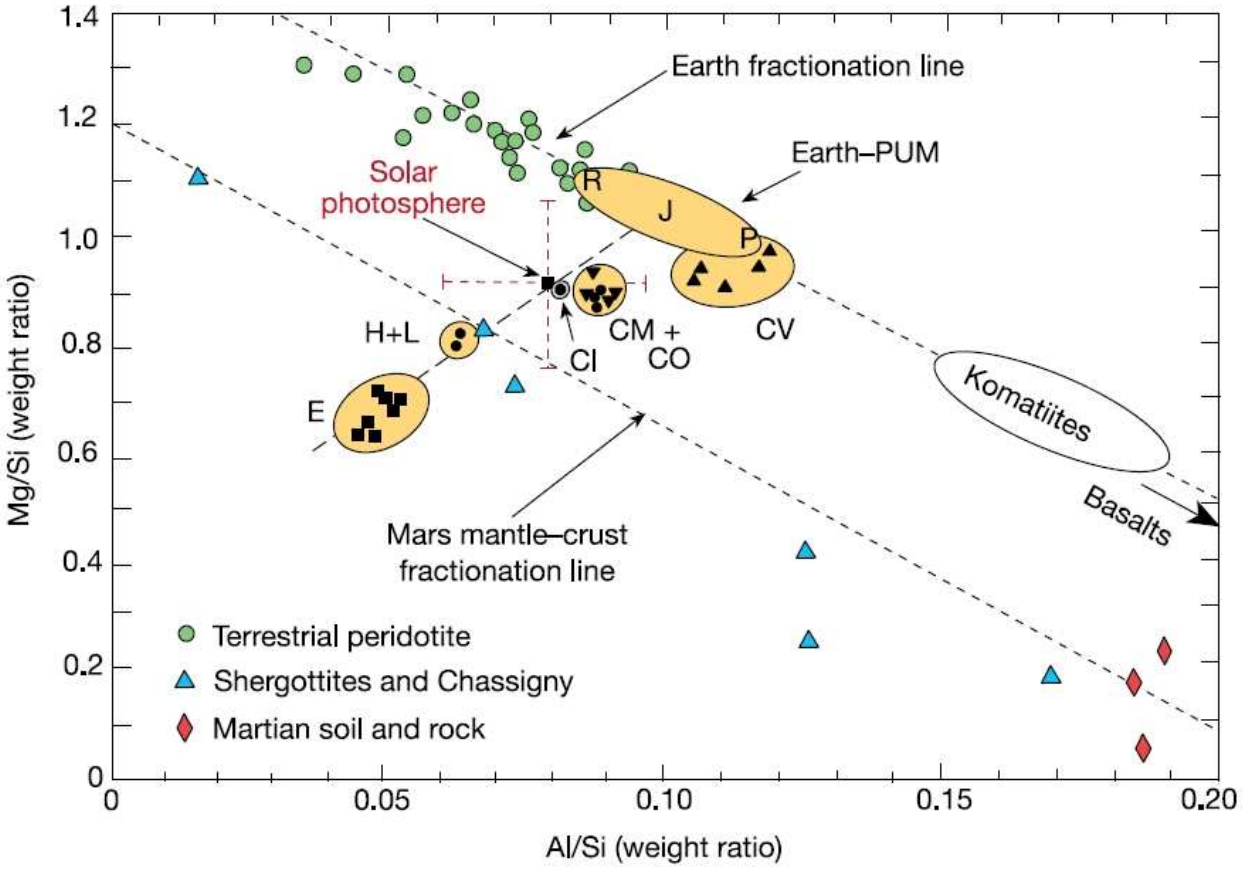

Figure 1.1. Mg/Si and Al/Si abundances of primitive material in the inner solar system; eclogite (E), ordinary (H, L) and carbonaceous (CI, CM, CO, CV) chondrites, primitive upper mantle (PUM) [4].

Primitive bodies in the solar system serve as reliquaries for the oldest materials that formed out of the solar nebula, but understanding their sources and the processes that created them requires a complexity of analysis that can only be achieved in controlled laboratory settings [5]. The analysis of recovered meteorites has raised many questions concerning the asteroids that produced them. Over the last four decades, data concerning the composition of these bodies has been mainly limited to spectra and albedo observations either by orbiting telescopes like the

Hubble Space Telescope, or by passing spacecraft like Galileo and Deep Space 1 [6]. These direct observation methods have provided valuable information concerning the locations and general characteristics of many asteroids, but compositional information has been questioned due to various physical processes that are recognized to occur on the surface of asteroids. Shifts in the apparent spectra of rocky bodies can be caused both by impacts (shock darkening) and space weathering which red-shifts the spectra of surface material [7][8]. This alteration of surface materials was discovered during the earliest and arguably most successful sample return missions during NASA's Apollo program.

If success is measured by the amount of sample material returned to Earth, the Apollo program, most noted for being the first exploration series to land humans on another rocky body, would be considered the most successful sample return missions to date. Between the summer of 1969 and winter of 1972, Apollo astronauts gathered and returned more than 300 kg of lunar material. While NASA employed human beings to collect material from the Moon, the Soviet's Luna program became the first automated system to return samples collected from a minor body, albeit in much smaller quantities. Figure 1.2 compares the return yields between the Apollo and Luna programs [9], and at first glance it seems obvious that manned sample return missions allow for the greatest collection of materials; however, manned missions are vastly more expensive, and current technology limits our ability to ensure the survivability of astronauts beyond low Earth orbit for extended periods of time.

The Apollo and Luna programs both employed soft-landing techniques, requiring the expenditure of considerable amounts of fuel to safely arrive on the Moon's surface, and additional propellant to ascend once collection efforts were completed. These maneuvers significantly increase a mission's ΔV budget, and require flawless execution to ensure the

survival of sensitive instrumentation. Soft-landing on a minor body like a moon presents major technical challenges, but attempting the same Entry Descent and Landing (EDL) methods on a gravitationally negligible body is even more difficult as demonstrated by the recent Rosetta mission to Comet 67P/Churyumov-Gerasimenko[10].

Mission name	Location	Mass returned (kg)	Date returned
Apollo 11	Mare Tranquilitatis	21.6	24 July 1969
Apollo 12	Oceanus Procellarum	34.3	24 November 1969
Luna 16	Mare Fecunditatis	0.10	24 September 1970
Apollo 14	Fra Mauro (Mare Imbrium)	42.3	9 February 1971
Apollo 15	Hadley Rille/Appenine Mts	77.3	7 August 1971
Luna 20	Apollonius Highlands	0.03	25 February 1972
Apollo 16	Descartes Highlands	95.7	27 April 1972
Apollo 17	Taurus-Littrow/Mare Serenitatis	110.5	19 December 1972
Luna 24	Mare Crisium	0.17	22 August 1976

Figure 1.2. Lunar sample return yields for the Apollo and Luna programs [9].

Figure 1.3. Artist's concept of the Philae lander after separating from the Rosetta spacecraft to begin a soft-landing EDL; Comet 67P/ Churyumov-Gerasimenko imaged by Rosetta's navigational camera [11].

Having traversed more than six billion kilometers over the course of a decade, the Philae lander separated from its mothership, Rosetta, on November 12, 2014. In order to conduct its full suite of experiments on the comet's surface, Philae was designed to latch on to the comet through the use of a series of harpoons and ice screws. The failure of these systems to deploy resulted in the solar powered lander bouncing across the surface of the comet twice, coming to rest in an area it was incapable of recharging its batteries in, and after only 60 hours of operation the system went into hibernation and was not heard from again until sending an 85 second message back to Earth on June 13, 2015 [12]. Despite the setbacks, the Rosetta mission has provided new information concerning the comet and although it was not a sample return mission, difficulties during its operation highlight the extreme challenges that soft-landing an automated spacecraft on a primitive body presents.

To circumvent difficulties in keeping a lander on the surface of an asteroid, some sample return missions have utilized a touch-and-go approach. In these scenarios, sample retrieval is conducted as the spacecraft briefly contacts the surface of the sampling target, collecting a few grams of surface regolith before moving on. NASA's OSIRIS-REx spacecraft will employ this approach in 2019 to gather materials from asteroid 101955 Bennu by deploying its Touch-And-Go Sample Acquisition Mechanism (TAGSAM), shown in Figure 1.4. During contact with the surface, the TAGSAM will use a burst of nitrogen to blow regolith through a collecting sieve, and lab testing indicates that the method is capable of gathering more than 60 grams of material [13]. The concept is not dissimilar to one attempted by JAXA's Hayabusa sampling of asteroid 25143 Itokawa in 2005, except that instead of using a nitrogen flushing system the spacecraft fired tantalum pellets at 300 m/s to collect the resulting ejecta inside its sampling mechanism [16]. Hayabusa demonstrated that touch-and-go sampling is possible, despite having crash-

landed on Itokawa during a sampling attempt and collecting less than 1 mg of material [17]; however, touch-and-go sampling limits collection to surface regolith and as such, Hayabusa2 (Figure 1.5) will deploy a kinetic impactor at the surface of asteroid 1999 JU3 in 2019, creating an artificial crater and collecting samples from greater depths than its predecessor [18]. The touch-and-go method of sample return avoids the problems of attaching a spacecraft to an asteroid and helps to reduce a mission's ΔV budget, but still represents substantial risk to the spacecraft due to the close proximity the vehicle must get to the primitive body in order to complete sampling.

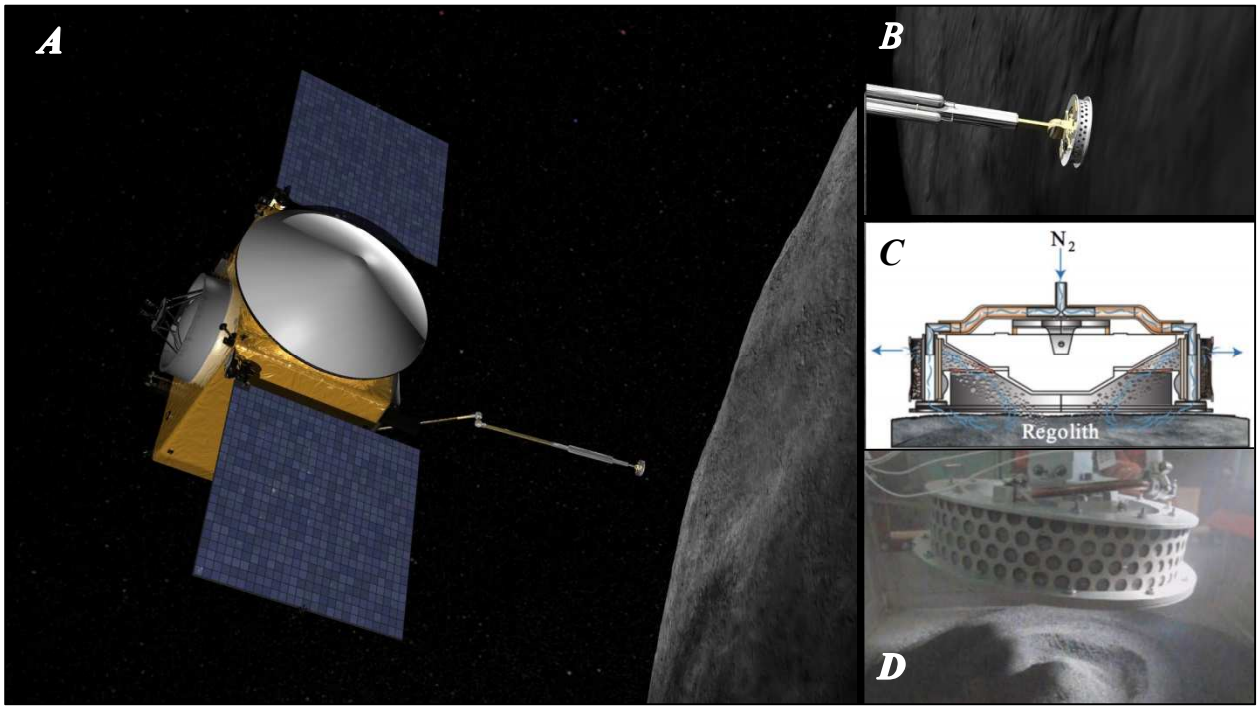

Figure 1.4. (*A)* Artist's concept of the OSIRIS-REx spacecraft deploying the TAGSAM instrument, (*B*) close-up of the TAGSAM head [14]; (*C)* schematic showing the TAGSAM Nitrogen flush method of sample collection, (*D*) laboratory testing of the TAGSAM head [15].

Another method used in sample return missions avoids direct contact with the targeted body completely. NASA's first sample return efforts after Apollo 17 was the Genesis mission, (Figure 1.6) designed to characterize and sample the solar wind using a halo orbit around

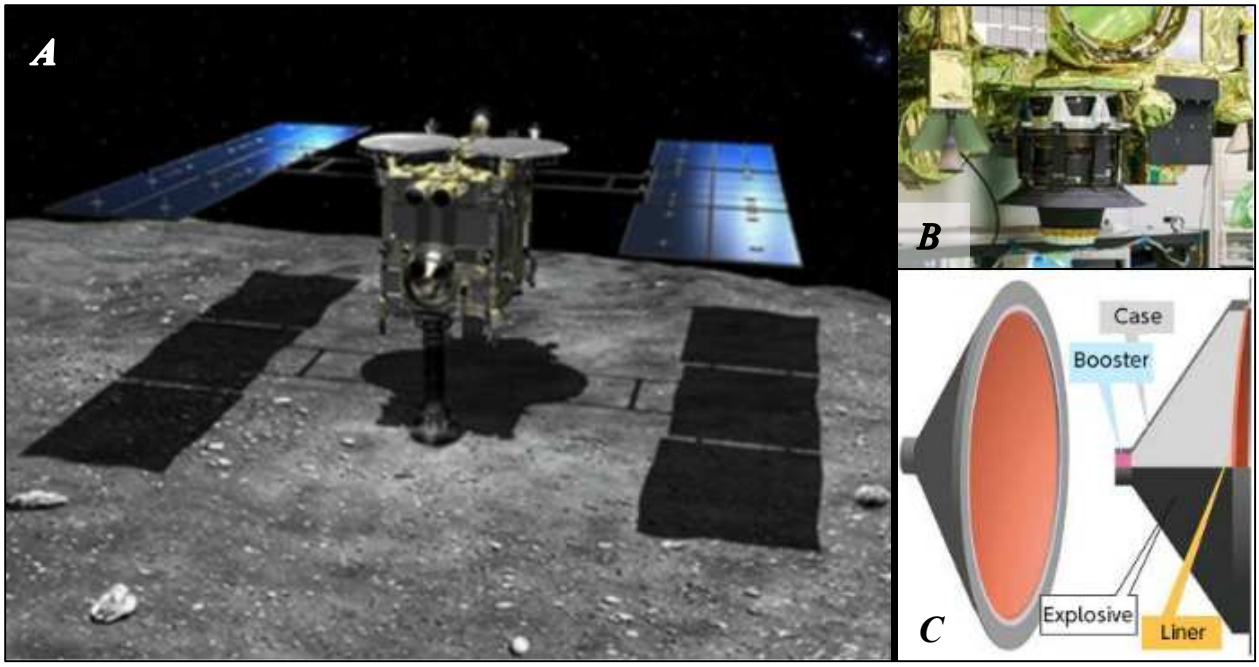

Figure 1.5. (*A*) Artist's concept of Hayabusa2 during touch-and-go sampling, showing its sampler mechanism (SMP) deployed and in contact with the asteroid, (*B*) the SMP onboard Hayabusa2 in its stowed configuration, (*C*) diagram showing the Small Carry-on Impactor (SCI) that will use explosives to reach an impact velocity of 2 km/s in order to facilitate the subsurface sampling of asteroid 1999 JU3 [18].

Lagrange point 1. The spacecraft gathered samples using collector arrays from late 2001 to spring of 2004, but the failure of its parachutes to deploy during Earth re-entry in September 2004 caused the Sample Return Capsule (SRC) to impact the landing zone at more than 86 m/s, resulting in the loss and contamination of significant amounts of sample material [19]. In contrast, the Stardust spacecraft (Figure 1.7), sent to collect samples from Comet 81P/Wild 2, enjoyed a much better success.

Launched in early 1999, the Stardust mission first collected samples of interstellar dust in 2000, and again in 2002 following an Earth gravity assist trajectory. The mission's flight team performed a close flyby of asteroid 5535 Annefrank, using the opportunity as an engineering test of ground and spacecraft operations prior to intercepting Comet 81P/Wild 2 in 2004, where it

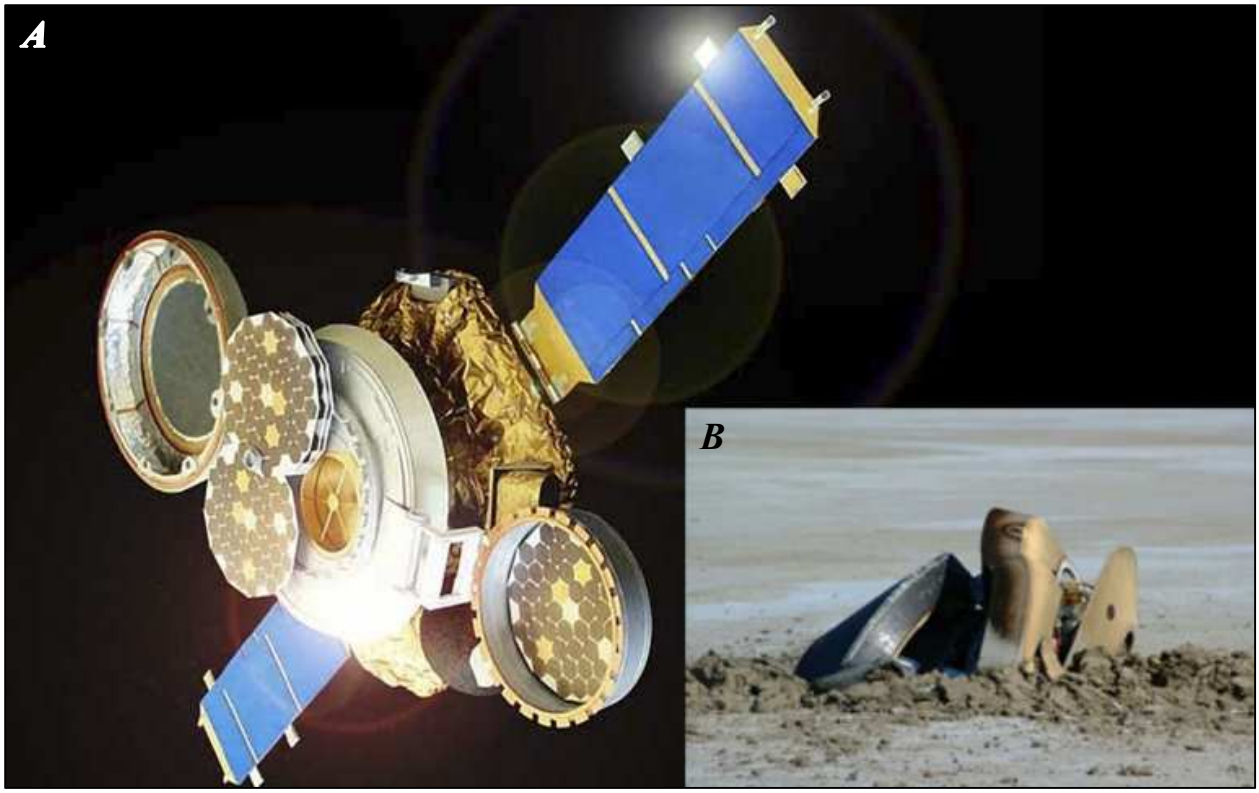

Figure 1.6. (*A*) Artist's concept of Genesis with its collection arrays deployed, (*B*) the impacted SRC [19].

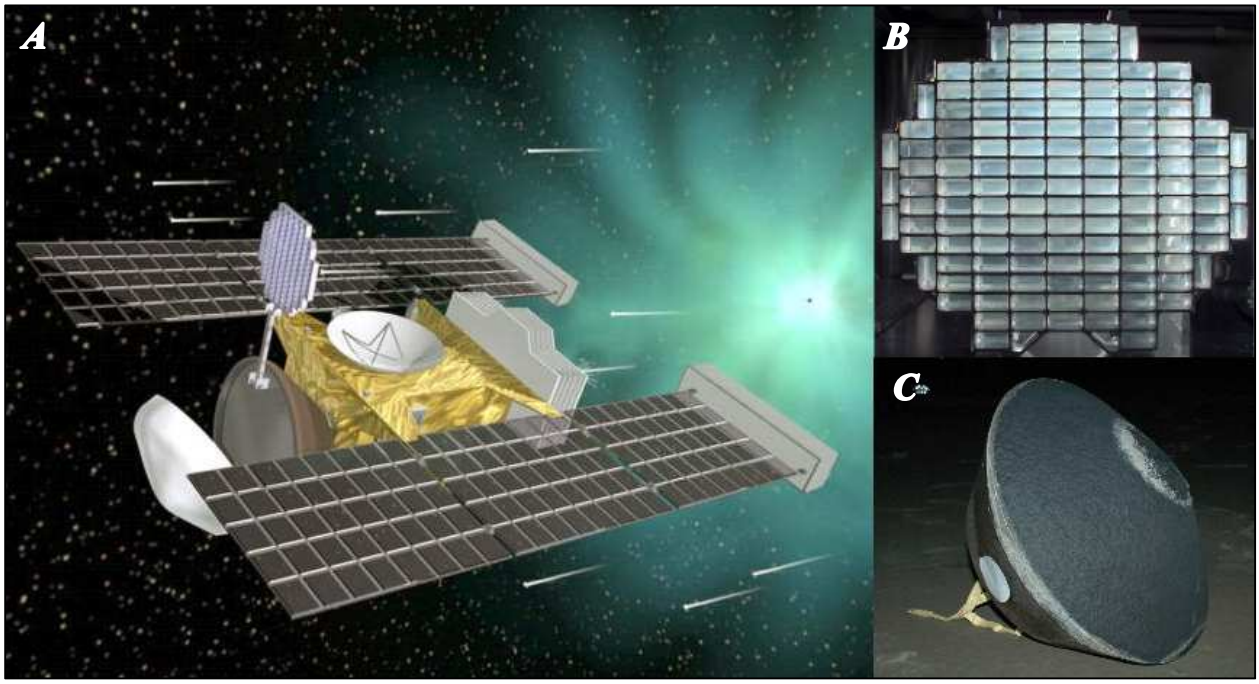

Figure 1.7. (*A*) Artist's concept of the Stardust spacecraft approaching Comet81P/ Wild 2 with its Collector Grid deployed, (*B*) the Aerogel filled Collector Grid prior to integration, (C) the SRC after successfully landing [20].

flew through the halo of gases and dust at the head of the comet [20]. The spacecraft used an Aerogel filled grid to collect materials thought to pre-date the birth of the Sun, and their successful return to Earth in 2006 has provided new insights into our solar system.

The aforementioned missions highlight the difficulties associated with sample return missions. No-contact methods that protect the spacecraft are not easily applied to most primitive bodies and touch-and-go techniques limit collection to altered surface materials, while soft-landing missions require considerably more propellant mass and increases to a mission's ΔV budget. Penetrators deployed from a passing spacecraft could reduce a sample return mission's ΔV since no additional expenditure of propellant would be required for descent/ascent on a primitive body, and adequate distances between spacecraft and the impacted target would prevent impact ejecta from damaging the spacecraft, but to date no penetrators have been intended for sample return missions.

1.3 Penetrators and Space Exploration

The lineage of planetary penetrators can be traced back to World War II and the development of ground penetrating munitions. The hardening of military fortifications was augmented by their construction at ever increasing depths below the surface, dictating advances in the weapons intended to destroy them. These early bunker-busters (Figure 1.8*A*) were large and heavy to provide effective penetration, requiring their deployment at high altitudes in order to maximize their impact velocity. Over the following decades the scale of these systems decreased allowing their application toward intelligence gathering as well, such as the USAF Igloo White Program (Figure 1.8*B*). These espionage penetrators demonstrated the ability for sensitive instrumentation to survive and operate after 2000 g impacts, and the systems were examples of

the application of early data compressing technology designed to minimize communication and bandwidth requirements [21].

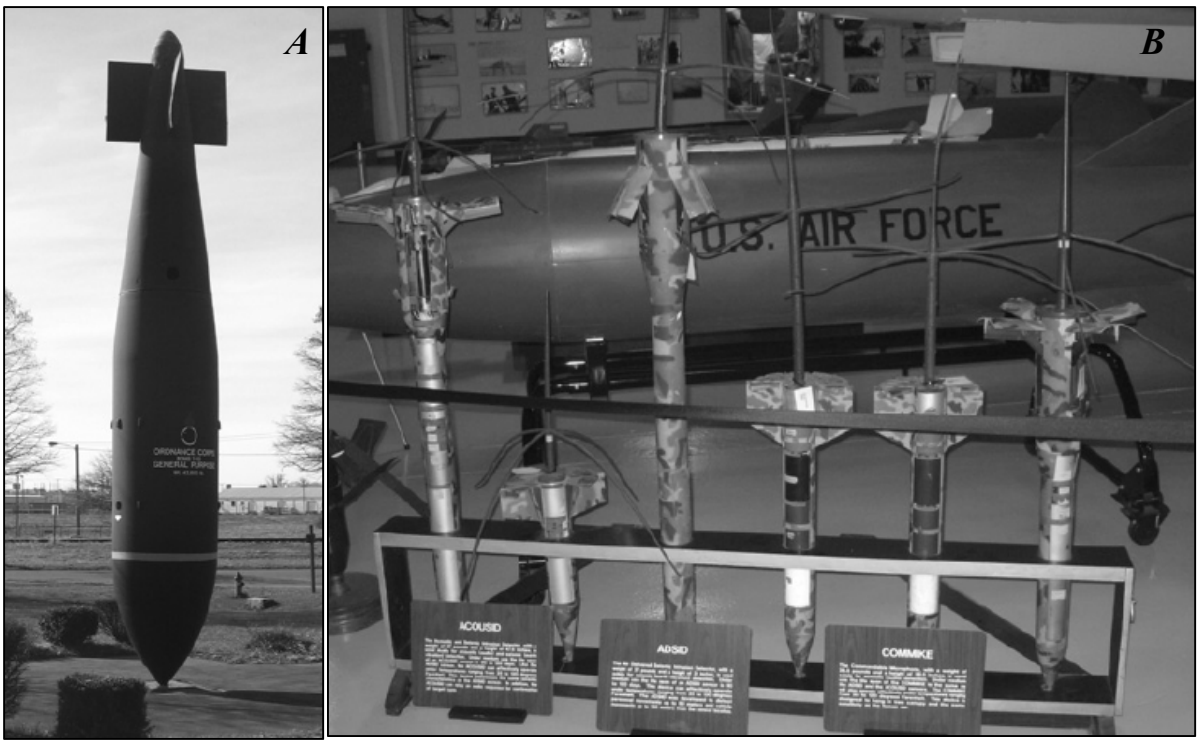

Figure 1.8. (*A*) The T-12 "Cloudmaker", (*B*) instrumented penetrators from the Igloo White Program [21].

The use of penetrators for space exploration was proposed as early as 1969 with suggestions that a Mars penetrator be used in conjunction with the Viking mission to search for subsurface water [21]. Over the following decades, multiple design proposals for embedding instrumentation during a Martian mission were brought forward given the limitations orbiting spacecraft and landers have in conducting surface observations. The Mars-96 penetrator, shown in Figure 1.9*A*, intended to deliver instrumentation for geophysical, meteorological, and compositional in situ analysis of the Martian environment [22]. The Deep Space 2 (DS-2) mission probes (Figure 1.9B) were the first planetary penetrators sent to Mars, carried by the Mars Polar Lander (MPL); however, as the spacecraft entered Mars' atmosphere, anomalies occurred during entry and neither the MPL or DS-2 probes were ever heard from again [23].

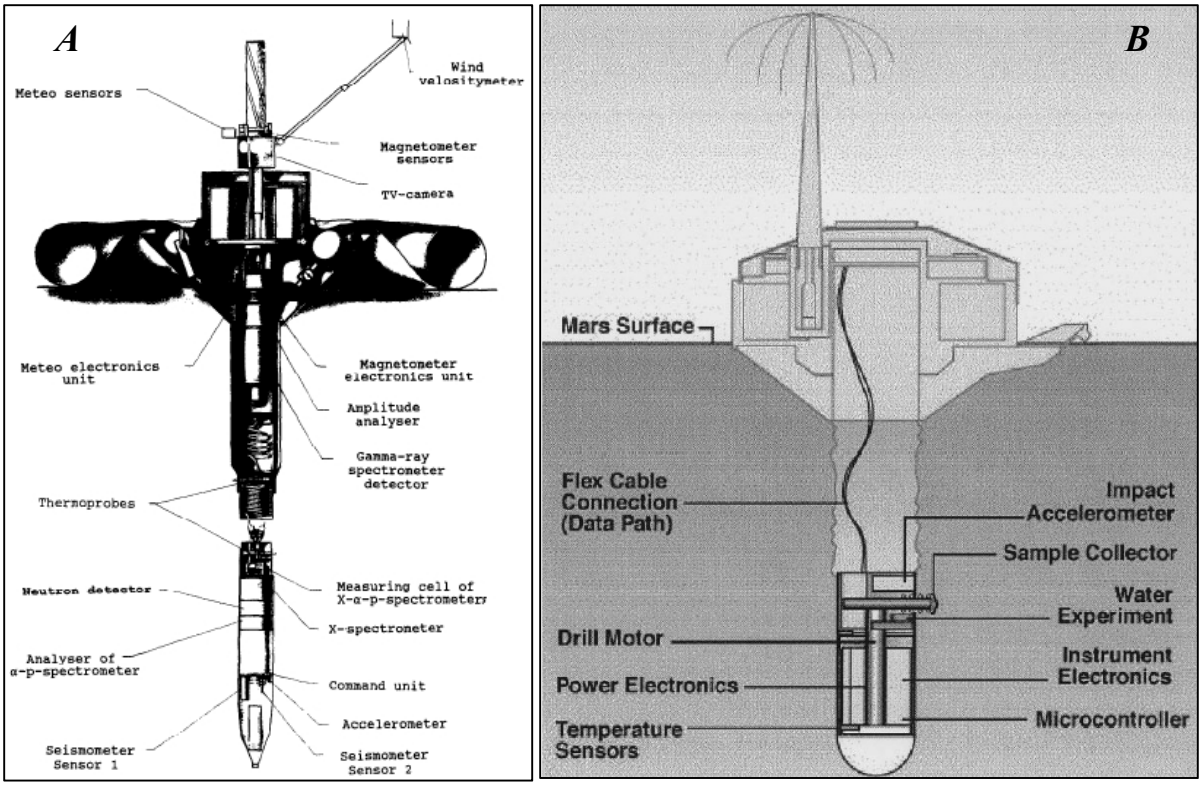

Figure 1.9. (*A*) Schematic for the Mars-96 penetrator [22], (*B*) schematic for the DS-2 probe [24].

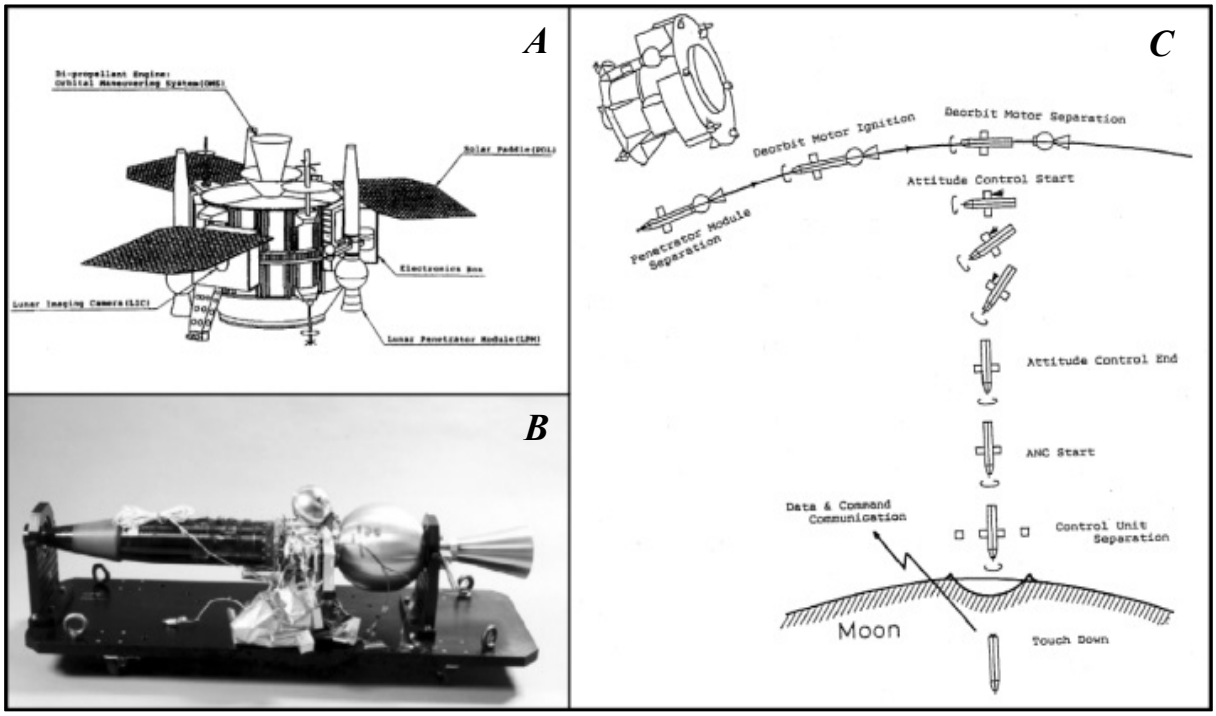

Figure 1.10. (*A*) Illustration of JAXA's LUNAR-A spacecraft [25], (*B*) a LUNAR-A LPM [21], (*C*) diagram depicting LUNAR-A penetrator deployment [26].

Embedding instrumentation in the surface of Mars is complicated by the planet's atmosphere, since aerodynamic affects need to be considered during EDL. Most minor bodies in the solar system are devoid of any atmosphere, making the use of penetrators for scientific investigation easier. The LUNAR-A mission (Figure 1.10) intended to use three Lunar Penetrator Modules (LPMs) to further our understanding of the origin and evolution of the Moon. The LPMs, designed to impact around 275 m/s to a depth of about 2 meters, carried highly sensitive seismometers and heat probes to collect data that would be transmitted back to Earth via the orbiting spacecraft every 15 days [26]. The LPMs would separate from their orbiting mothership one at a time, and use solid state motors to achieve velocities low enough to deorbit and free fall to the lunar surface. The process was planned to take roughly one month to deploy all LPMs, embedding two on the near side and one on the far side of the Moon. Unfortunately, development of the LPMs took much longer than planned resulting in components populated in the mothership becoming obsolete, and the project was canceled in 2007 [27].

Chapter 2. SAMPLE RETURN SYSTEMS FOR EXTREME ENVIRONMENTS (SARSEE)

2.1 SARSEE MISSION CONCEPT

Over the centuries that humanity has observed the heavens, the major bodies (planets) have received the lion's share of attention, but their numbers represent only a small portion of the bodies that inhabit our solar system. To date we have identified more than 150,000 asteroids in the main belt alone [28], but difficulties in collecting samples has resulted in returning limited material from only one, asteroid 25143 Itokawa [29]. Table 2.1 shows a representative comparison of escape/orbital velocities for select minor bodies that could serve as potential

Table 2.1. Representative comparison of escape and orbital velocities of select minor bodies [30].

PLANETOID	MASS	RADIUS	V_{esc}	V_{orb}
	(10^{20} kg)	(km)	$(2GM/R)^{1/2}$	$(3GM/4R)^{1/2}$
208 Lacrimosa	0.00043	20.5	16.7	8.8
Chiron	0.04	90	77.0	45.3
Mimas	0.37	196.5	159.5	95.9
Enceladus	1.10	252	241.3	145.6
Pallas	2	272	321.7	194.3
1994VK8	4	389	370.4	224.6
Vesta	3	263	390.1	235.5
Tethys	6	531	394.7	240.0
Ceres	10	487	523.4	318.1
Dione	11	561	511.4	311.1
Iapetus	18	734	572.0	348.5
Charon	17	586	622.1	378.5
Rhea	23	763	634.1	386.4
Titania	35	789	769.3	468.9

candidates for the SaRSEE mission concept. The following mission scenario takes advantage of these smaller velocities and avoids hazards experienced in earlier missions by protecting the main spacecraft by maintaining a safe distance from the targeted body. Additionally, the use of penetrators for sample collection allows for subsurface sampling of materials unaltered by space weathering, while tether technology used for retrieval reduces a mission's ΔV budget since no propellant expenditure is required for landing and ascending from the surface of a primitive body.

In the SaRSEE mission concept, the spacecraft deploys a tethered penetrator as it approaches the sampling target, shown in Figure 2.1. The penetrator descends to the target surface, using the momentum imparted by the spacecraft to generate the necessary impact velocity (<700 m/s) to penetrate more than one meter below the surface. During the impact, feed ports in the nose cone allow material to flow up through the penetrator to a SRC at the aft of the penetrator (Figure 2.2). Energy absorbing material protects the SRC from the impacting forces

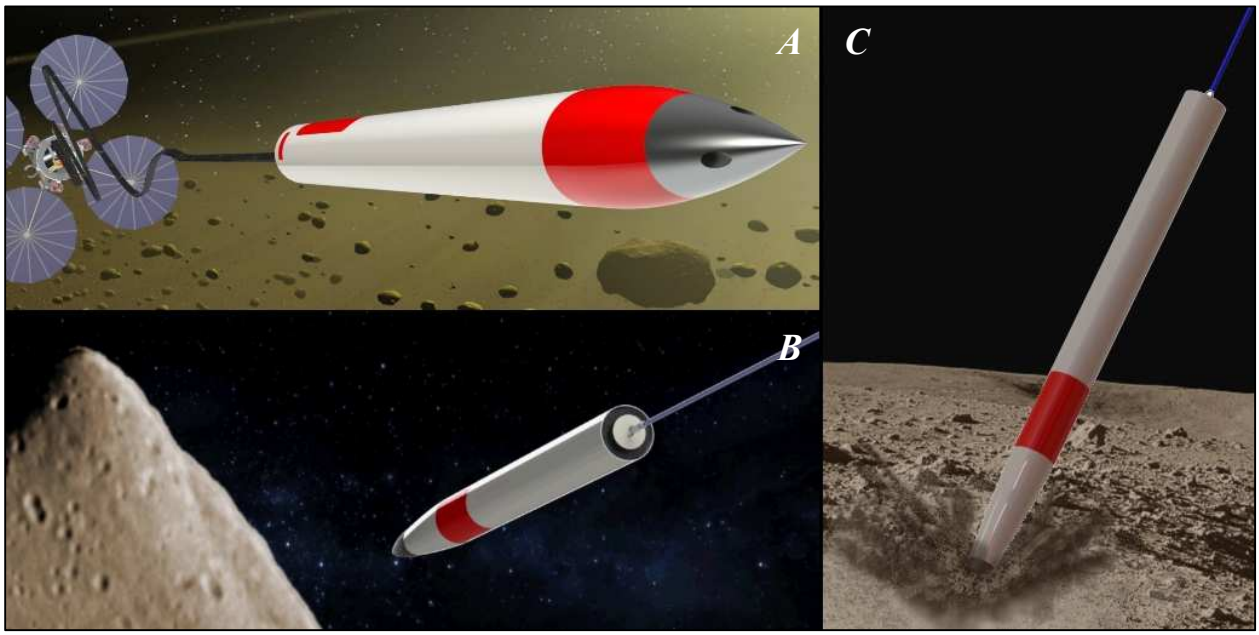

Figure 2.1. (*A*) Artist's concept of the spacecraft deploying a tethered penetrator,(*B*) followed by the descent to the target's surface, (*C*) and the resulting impact.

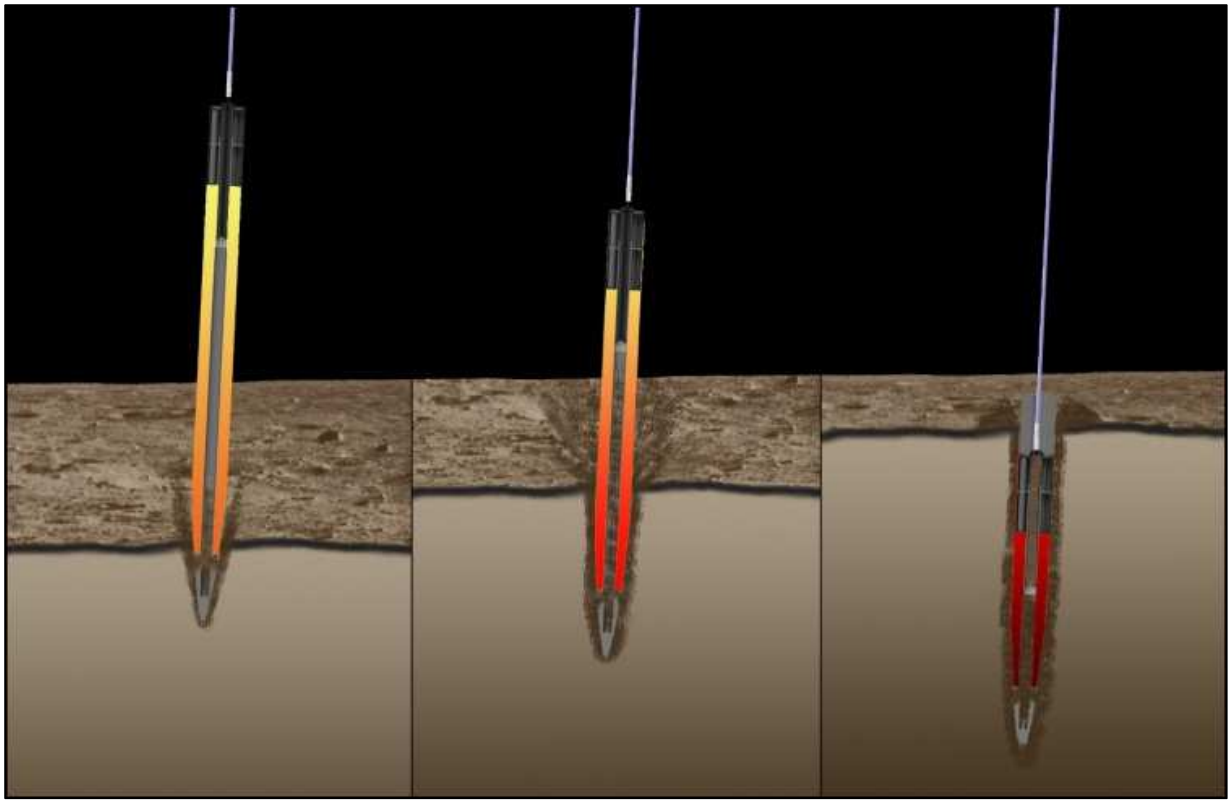

Figure 2.2. Artist's concept of sampling during the impact process. Material flows through the penetrator to a SRC at the aft of the penetrator.

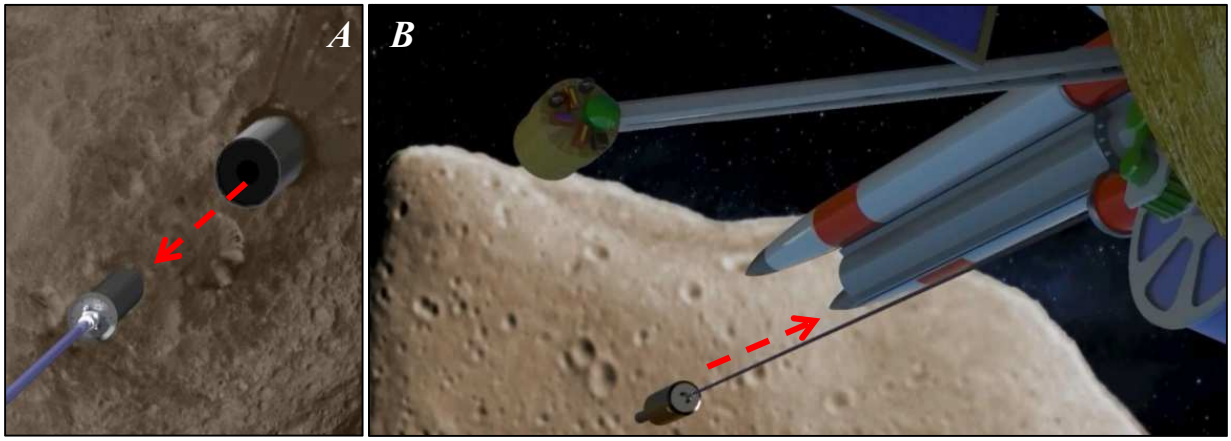

Figure 2.3. (*A*) Artist's concept showing the SRC extraction that leaves the rest of the penetrator in situ, (*B*) and its recovery to the spacecraft via the tether without requiring the spacecraft to land.

while the main body of the penetrator is compressed along its length. The SRC, still tethered to the spacecraft, is ejected during collection by the flow of incoming sample material, and is reeled back to the mothership for containment; alternately, the SRC could be released by the spacecraft on an Earth return trajectory. By using the kinetic energy of the spacecraft, the SaRSEE concept reduces the mission's ΔV requirements, and as such offers better mass ratios that lower the expense of sample return missions and allow for subsurface sampling with estimated return yields of about 3-5 kg per impact. Comparisons between applied tether technology and chemical propulsion mass ratios are shown in Figure 2.4.

SaRSEE's reduced mass ratios open the potential to sample multiple targets of interest along a well-planned trajectory, or the ability to sample multiple locations on a single target depending on whether the spacecraft performs a fly-by of a primitive body (which may be ideal for smaller members of the population) or orbits the object. An additional advantage the use of penetrators for sample return missions offers is the variability in the spacecraft that could deploy them. Figure 2.5 shows configurations for two early concepts: (*A*) a revolver-style loading system in which multiple penetrators can be cycled through, connecting to a single tether before deployment for the recovery of each SRC; (*B*) a single, shared-guide rail concept in which each penetrator is connected to an independent tether. The same sampling concept could also be applied terrestrially, without the need for a spacecraft, for application in environments too hostile to risk sending a human being into. The ability to collect irradiated samples in the first few days following the containment failure at the Fukushima I Nuclear Power Plant in 2011 could have eliminated the need for volunteers to enter the hazard zone, for example. There has also been interest in using the technology for collecting samples from active volcanic eruptions that are too dangerous for scientists to enter.

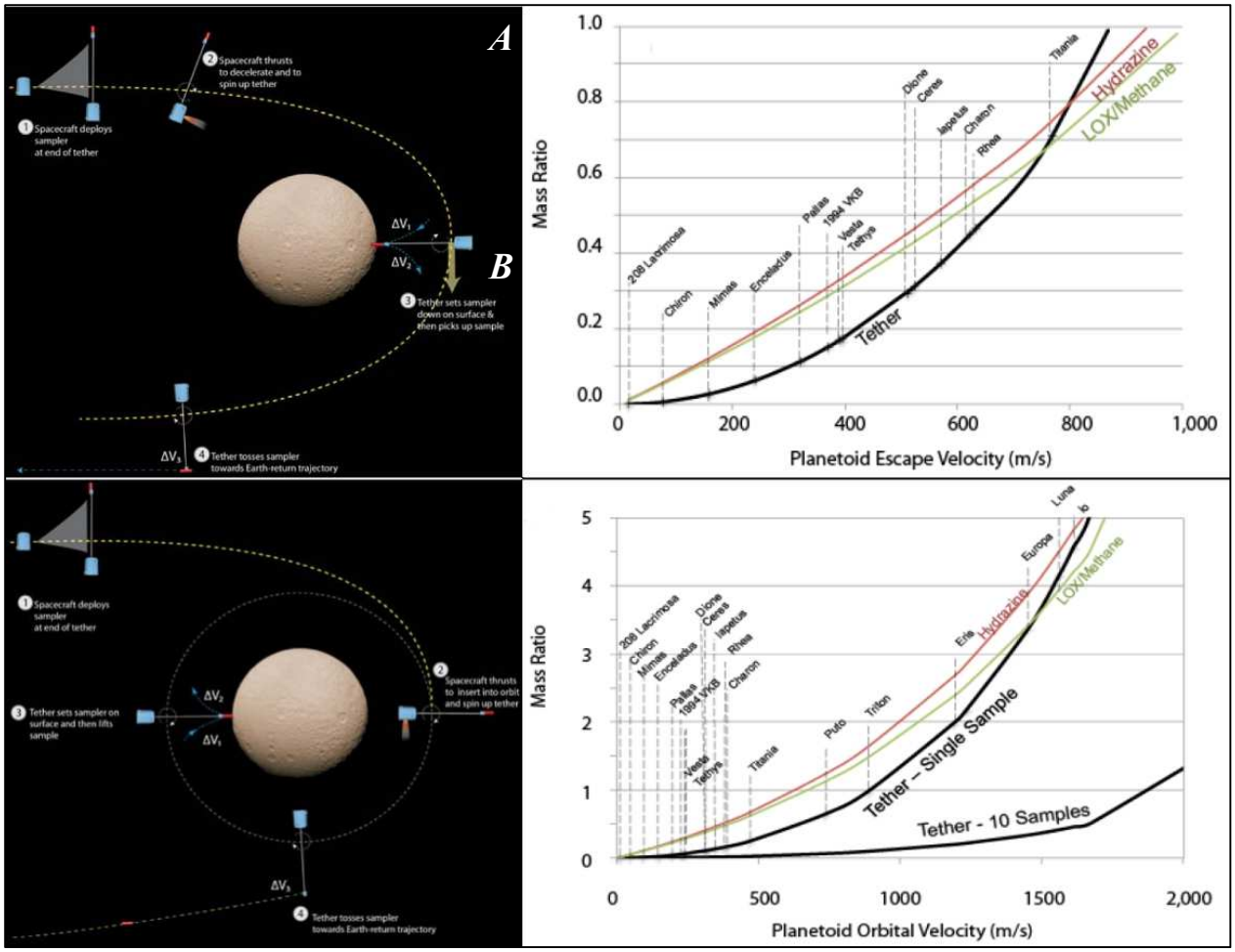

Figure 2.4. (*A*) Conceptual schematic for a fly-by SaRSEE mission with mass ratio comparison; (*B*) mission concept for orbital sampling with mass ratio comparison showing multiple samples collected [30].

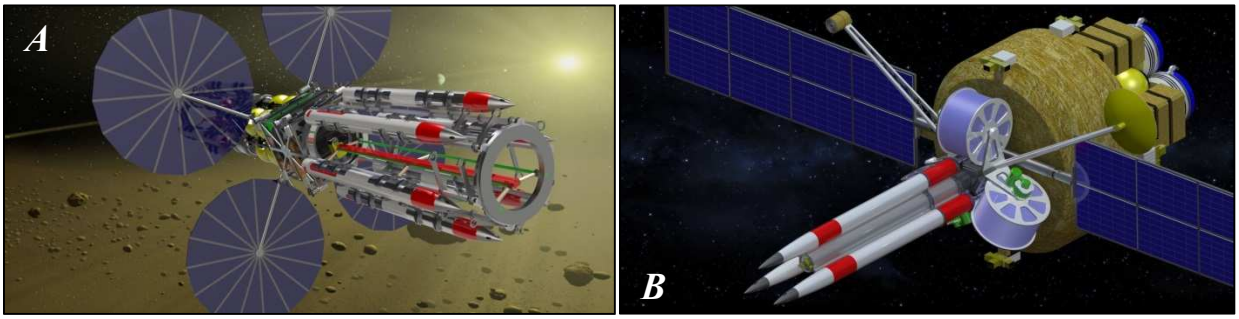

Figure 2.5. (*A*) A revolver-style flight system concept equipped with at least six penetrators that share a single tether, (*B*) a shared-guide rail flight system concept equipped with three penetrators, each with an independent tether. Both systems rely on electric propulsion for cruise and attitude control, and are solar powered for traversing the inner solar system.

2.2 PENETRATOR DESIGN

Inspiration for the design of the SaRSEE penetrator originated during annual field testing at Black Rock, Nevada, in March of 2012 by students enrolled in the Rockets and Instrumentation course offered at the University of Washington's Department of Earth and Space Sciences. The Aluminum Rocket Prototype (Figure 2.6) was the first attempt at integrating aluminum structures into the composite materials normally used by the class, consisting of a solid aluminum nose cone, and internal aluminum rib-and-stringer skeleton. While the rocket launched as expected, a power anomaly at apogee prevented the recovery charges from firing, resulting in a ballistic impact. During recovery, it was observed the motor casing was nearly ejected intact, and the

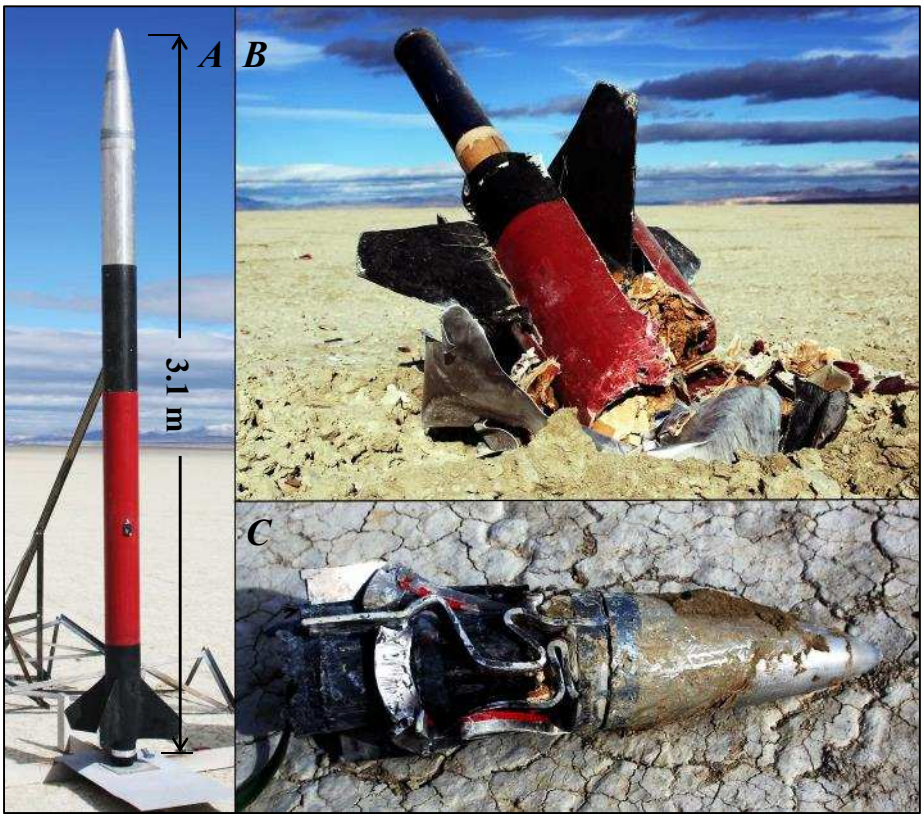

Figure 2.6. The Aluminum Rocket Prototype (ARP) inspired the design work that became the SaRSEE penetrator; (*A*) ARP pre-launch, (*B*) post-impact showing motor casing nearly ejected, (*C*) recovered nose cone intact with deformed stringers that absorbed the impact energy.

nose cone experienced no deformation. The rocket embedded to a depth of ~0.71 m, and while most of the airframe was destroyed, the rib-and-stringer infrastructure had absorbed much of the impact energy that resulted in minimal damage to the motor casing.

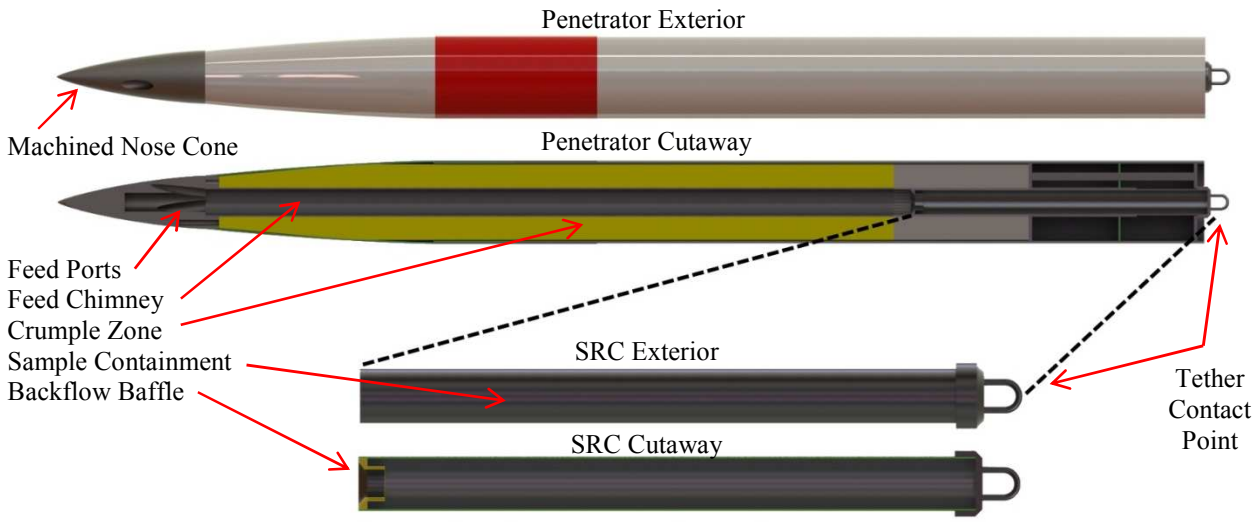

Figure 2.7. Simple schematic of the SaRSEE penetrator showing internal sections and the SRC.

Figure 2.7 shows the basic internal layout for the SaRSEE penetrator, consisting of the machined nose cone equipped with feed ports, the crumple zone where energy absorbing layers of composite materials surround the feed chimney, and the SRC that also serves as the tether contact point. Ejecta flows through the feed ports and up the chimney, collecting in the SRC, so development of energy absorbing materials was critical to ensure the SRC would survive the impact.

Honeycombed aluminum structures have a long history of use in aerospace applications given their high strength-to-weight properties, and as such were optimal candidates for use as light weight, energy absorbing structures in the penetrator's crumple zone. Early estimates calculated the material would need to endure 500 kN of force before total failure to protect the SRC during impact, so test samples using Hexcel® Hexweb® aluminum honeycomb material

were developed [30]. Compression testing was conducted using an Instron 5585H Series Floor Model Testing System capable of providing a maximum load of 250 kN for 75x75x16 mm test samples. When the honeycombed aluminum is compressed along the axis of the cells, the cell walls collapse in a concertina-like manner, and test samples were treated with various additives to fill the cell voids and increase the strength of the material (Figure 2.8). These additives were found to both increase the material's strength and its post-compression cohesion in that the

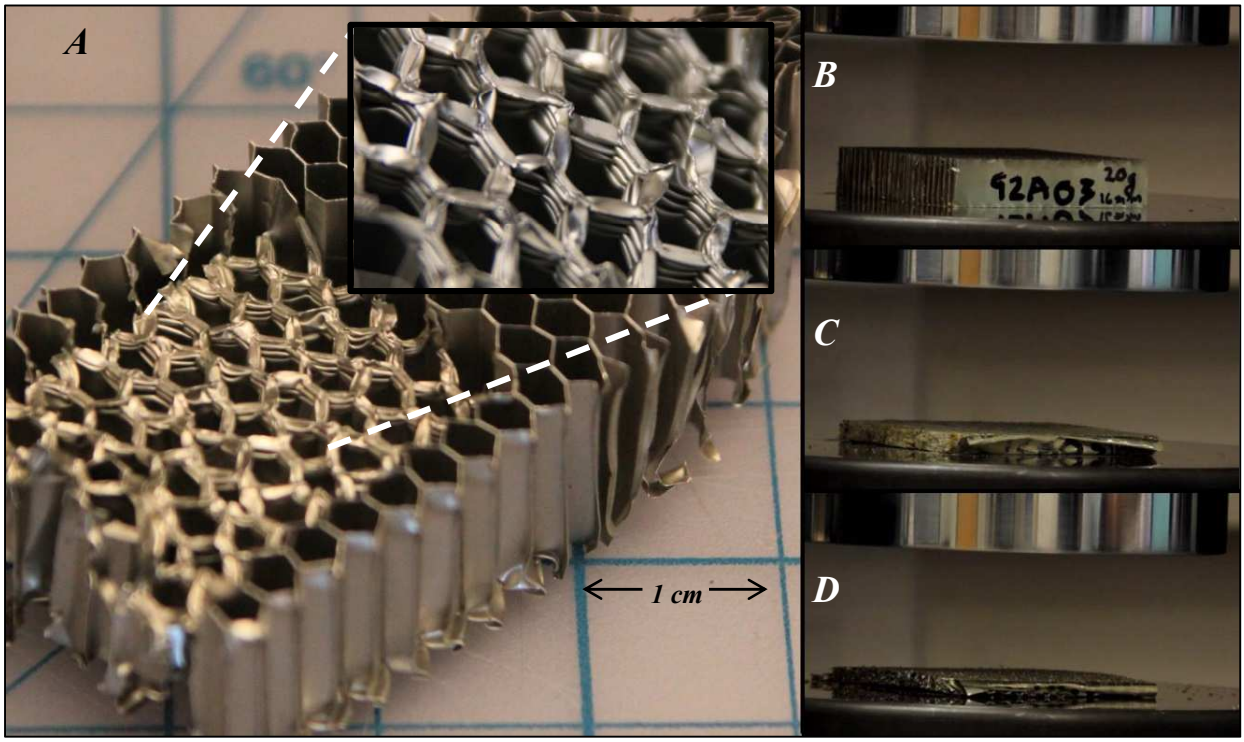

Figure 2.8. (*A*) Aluminum honeycomb cells collapse in concertina-like manner; (*B*) treated test sample prior to compression, (*C*) and after compression; (*D*) untreated sample after compression showing less resilience in both compressive displacement and material cohesion.

compressed treated samples did not crumble into smaller bits of debris like the untreated honeycomb material. A plot of the testing results for four of the samples is shown in Figure 22, while a description of the modifications made to the honeycombs for these tests is listed in Table 2.2.

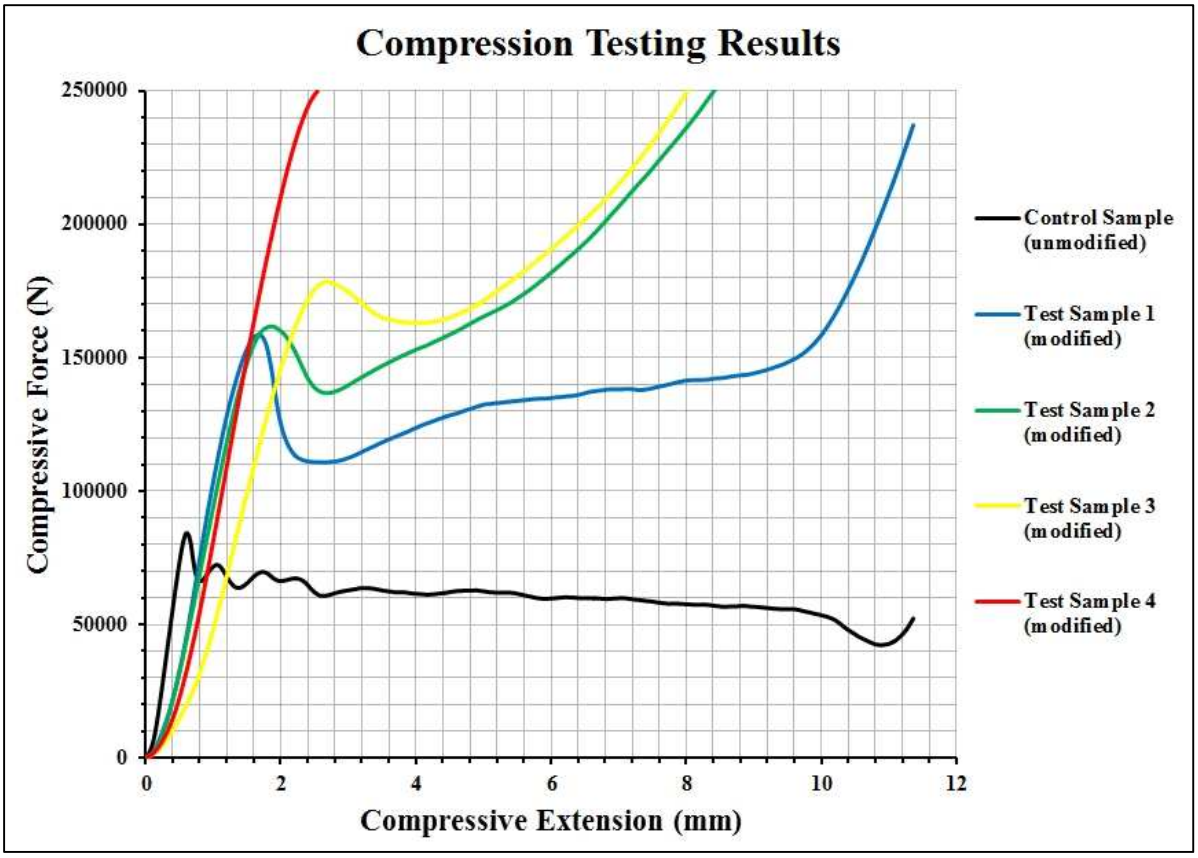

Figure 2.9. Comparative results from compression testing of four modified samples to the control sample. Sample 4 rapidly exceeded the Instron's loading capabilities; modified samples' behavior after reaching their initial yield threshold is very different from the control, rapidly increasing in strength as the material compresses.

Table 2.2. Sample modification descriptions, masses, and maximum compressive loads.

Hexcel® Sample (75x75x16 mm)	Modification	Mass	Maximum Compressive Load
Control Sample	none	20 gm	84.31 kN
Test Sample 1	Kevlar Putty 25.4 mm spacing	45 gm	237.13 kN
Test Sample 2	Foam epoxy	34 gm	250.50 kN
Test Sample 3	Kevlar Putty 12.7 mm spacing	50 gm	250.64 kN
Test Sample 4	Kevlar putty 6.4 mm spacing	65 gm	(unknown)

The addition of various fillers in the Hexcel® significantly increased the material's maximum compressive yield, and in most cases did not result in a substantial addition of mass. The material was integrated into the penetrator system to create a crumple zone (Figure 2.10) capable of protecting the SRC during impact, while a machined, solid nose cone allowed for adequate penetration.

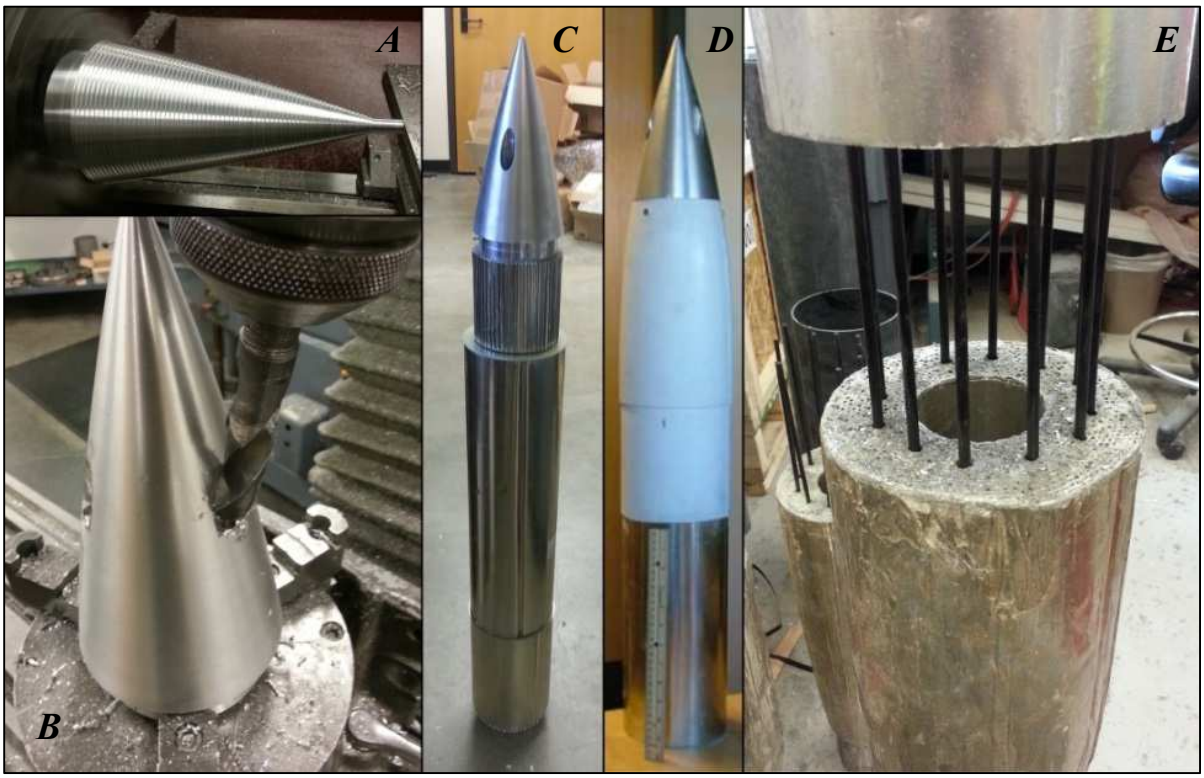

Figure 2.10. (*A*) Machining of the one of an aluminum nose cone, (*B*) and feed ports. (*C*) The nose cone and modified honeycombed aluminum, (*D*) and their integration into the rocket assembly. (*E*) Carbon fiber rods reinforced joints between sections of energy absorbing material to help resist shearing during impact.

Since the target material in for the first flight series was playa, aluminum was determined to be sufficient for field testing; two nose cones were designed to test the differences in penetration depth for different nose cone masses and geometries. Testing during subsequent

flight series required harder material for embedding in various soils and sandstone, so A2 Tool Steel was selected due to its relative ease in machining and its ability to be hardened to a Rockwell hardness ~62c. Additional design changes to the feed port geometry were made: one nose cone retained the triple, concentric feed ports, while the other employed a single feed port bored along the centerline of the nose cone. Figure 2.11 displays the four different nose cone designs.

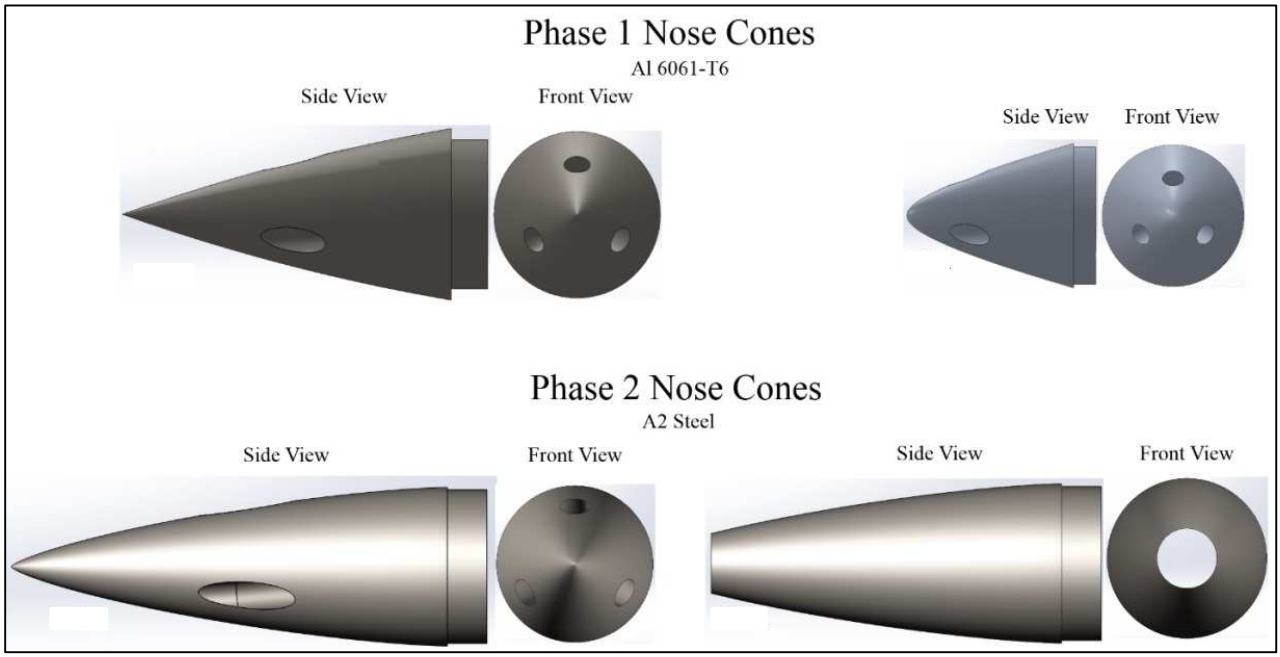

Figure 2.11. Comparison diagram showing the nose cone design for the first and second flight series.

During the second series of field tests, the flow of incoming sample material was experiencing a stagnation point shortly after entering the feed chimney (see section 3.2). SolidWorks' FloXpress Analysis Wizard was used to model flow velocities inside the nose cones, and results of these models is shown in Figure 2.12. A new nose cone design was created that combined two earlier iterations resulting in a hybrid feed port configuration: a single, tapered centerline port, and three off set ports. It is important to note that solid material flow cannot be modeled in SolidWorks; instead, water was selected as the medium to demonstrate

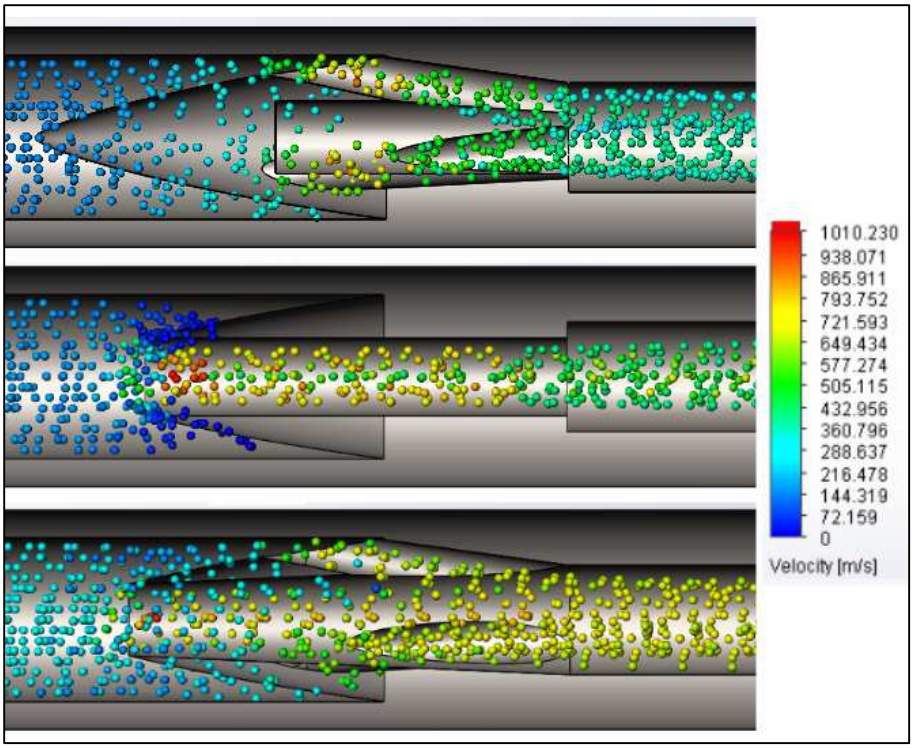

Figure 2.12. Relative flow model created in SolidWorks comparing the flow velocities between three feed port designs: the triple-port design (top), the single center port design (center), and the hybrid design (bottom). Relative flow velocity in the feed chimney is highest in the hybrid design; particle color designates velocity.

relative differences in internal flow velocities occurring in the three variants. Regardless, the modeling demonstrated the hybrid design allowed for the highest internal flow velocities. As such, a fourth evolution of the nose cone was produced, integrating the hybrid steel tip for penetration strength, with aluminum components to keep the final nose cone mass down.

Planetary penetrators using methods proposed in the SaRSEE concept require no propellant since they utilize momentum imparted from the spacecraft, and aeronautical concerns are minimal since primitive bodies have negligible atmospheres at best; however, testing penetrators on Earth require both propulsion and aerodynamic stability to reach the desired impact velocities. During the first flight series, a two stage, inline motor design was tested in the

Black Rock Desert. The boost stage was designed to lift the vehicle to apogee at about 1,500 meters, and separate from the second stage. The vehicle was then allowed to free-fall for about 200 meters to reach a velocity around 100 m/s before igniting the second stage motor, providing aerodynamic stability prior to ignition to ensure both a reasonable impact angle and to lower the risk posed to ground operations crews. Optimized tail fins provided passive stability during flight, and aerodynamic drag was reduced by covering the feed ports with layers of carbon fiber. Figure 2.13 shows a schematic of the first system.

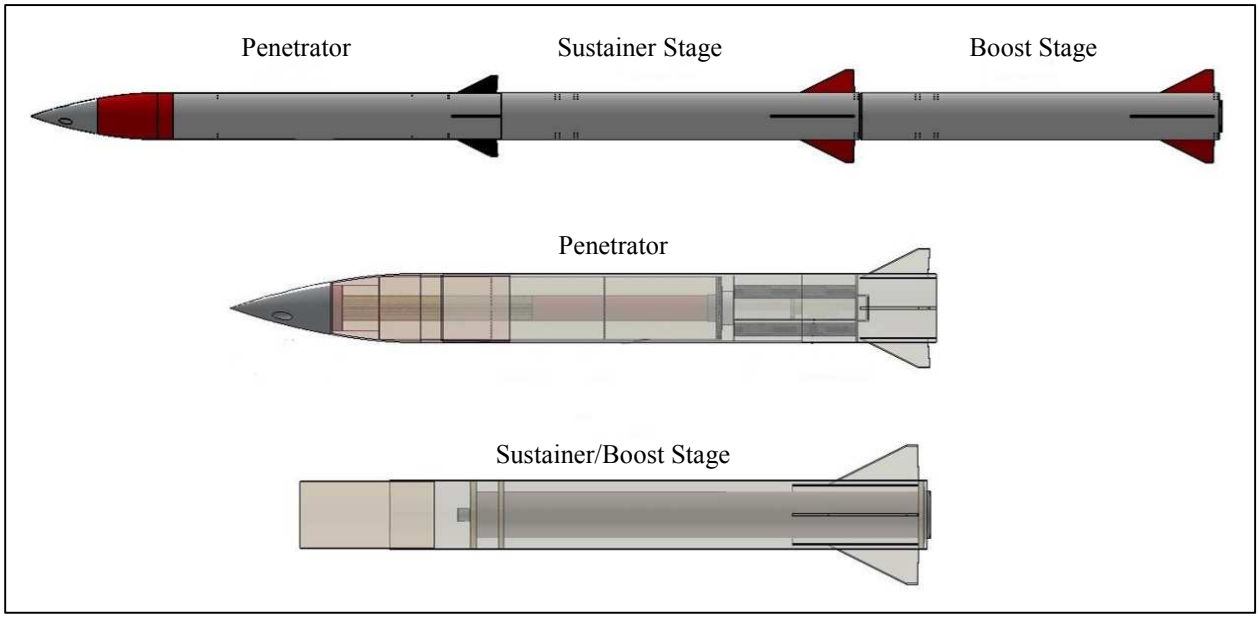

Figure 2.13. The first two-stage penetrator.

During subsequent flight tests, advances in the fabrication of clustered motor stages allowed for the redesign of the penetrator. Instead of a single, in-line motor, eight out-board motors were incorporated, reducing the overall length of the rocket. The out-board motors were integrated directly into the airframe of the penetrator and were designed to shear off during impact, preventing the motor casings from following the penetrator along the embedding vector. Figure 2.14 shows the updated penetrator design.

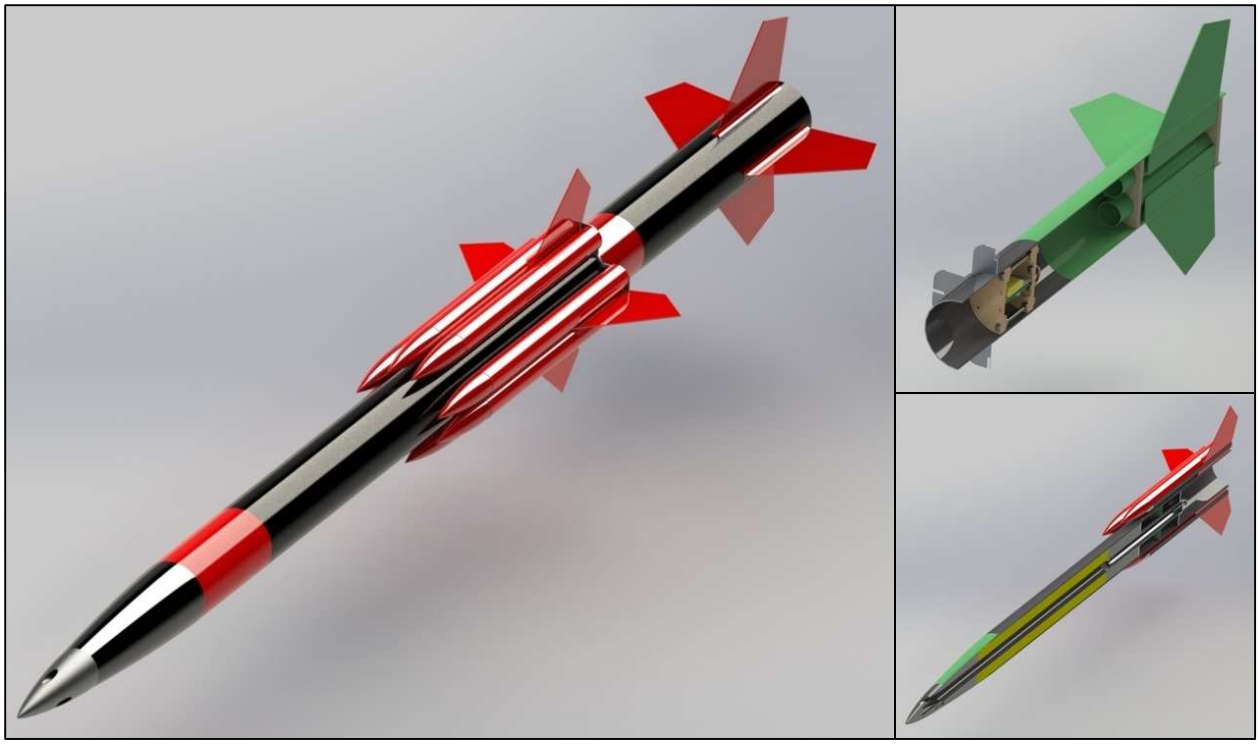

Figure 2.14. The two-stage penetrator showing the out-board motors, and cutaway views of the boost stage and penetrator; the sustainer stage was integrated directly into the penetrator airframe.

Chapter 3. FIELD TESTING

The evolution of moving from theoretical design to testing concepts in the field inherently reveals flaws in assumptions made early in the process, and professional aerospace organizations may spend years and millions of dollars refining a product to develop a finalized, fully functional system. Time and budgetary constraints allowed for only a precursory evaluation of the SaRSEE mission proposal, dominated by the proof-of-concept for the penetrator, and as such there remains extensive development needed for moving beyond Technology Readiness Level 3. Despite these limitations, the research conducted over the course of three years did in fact demonstrate the potential for the use of penetrators for sample return. Amateur rocketry methodologies adopted from the University of Washington's Department of Earth and Space Sciences rocketry program allowed for the rapid, in-house production of the penetrators to facilitate their fabrication under the financial and scheduling requirements.

3.1 BLACK ROCK, NEVADA

Initial testing for the SaRSEE penetrator was conducted during the annual trip to Black Rock, Nevada, for the Rockets & Instrumentation course offered by the University of Washington's Department of Earth and Space Sciences. Figures 3.1 through 3.4 represent only a portion of the work conducted during Phase I; for a full review of Phase I results, refer to the final NIAC report, "Sample Return Systems for Extreme Environments" [30].

The test flights in Black Rock demonstrated the penetrators' survivability during subsonic and supersonic impacts, and the ability of collecting sample material through the feed ports. Two test flights were conducted: the first test flight (Gravedigger 1) resulted in a

subsonic impact after which the penetrator was recovered nearly completely intact; the second flight (Gravedigger 2) demonstrated the sample collection via the feed ports in the nose cone.

Gravedigger 1 was the first evoloution of the SaRSEE penetrator, built from the designs shown in Figure 2.13 and Figure 3.1. The system utilized a two-stage rocket designed to use the first boost motor to lift the vehicle to apogee and first stage seperation. Once the rocket was aerodynamically stable, the second boost stage was supposed to ignite in order to create impact velocities around 500 m/s; however, a structural failure in the commercially supplied motor casing resulted in a premature seperation of the second stage and the penetrator. As such, impact velocities were lower than desired, and were estimated to be only around 180 m/s. Post flight analysis revealed the penetrator sustained no critical damage, but the impact velocity was insufficient to open the feed ports that had been sealed with carbon fiber so no sample was collected. Figure 3.2 shows the impact site, and the crossed-sectioned penetrator post-flight.

Given the difficulties experienced in the first flight, an alternate flight plan for Gravedigger 2 was employed. Instead of a traditional multi-stage flight, the penetrator was refit as a single stage rocket that was lifted to apogee via the use of two power sled kites. The system was lifted to an altitude of about 1,100 meters, and the exhaust plume of the motor was used to sever the connections to the kites. The flight can be seen in Figure 3.3. The major disadvantage to the alternate flight plan was that there was not a reliable way to separate the motor stage from the penetrator, and as such the motor continued under power down the impact shaft created by the pentrator. While most of the penetrator was incinerated, the nose cone survived and the feed successfully collected material during the impact, shown in Figure 3.4.

Figure 3.1. The first SaRSEE penetrator, Gravedigger 1, just prior to being loaded on the launch rail. The rocket employed an Aerotech M1850W (7,500 N-sec) in its black boost stage, and an in-line, Cesaroni N10,000 (10,347 N-sec) motor in the purple sustainer.

Figure 3.2. (*A*) During the flight of Gravedigger 1, the second stage motor casing failed during ignition when the forward enclosure sheared off. While the penetrator was blown clear, the resulting impact velocity was lower than desired (~180 m/s). (*B*) The impact created a clearly defined crater, with radial fractures in the playa, (*C*) and the penetrator embedded to a depth of 1.32 meters at an angle of ~30° off normal. (*D*) Post recovery examination of Gravedigger 1 revealed the impact resulted in almost no internal damage to the penetrator, but the impact velocity was too low to open the feed ports that had been covered with carbon fiber, so no sample was collected.

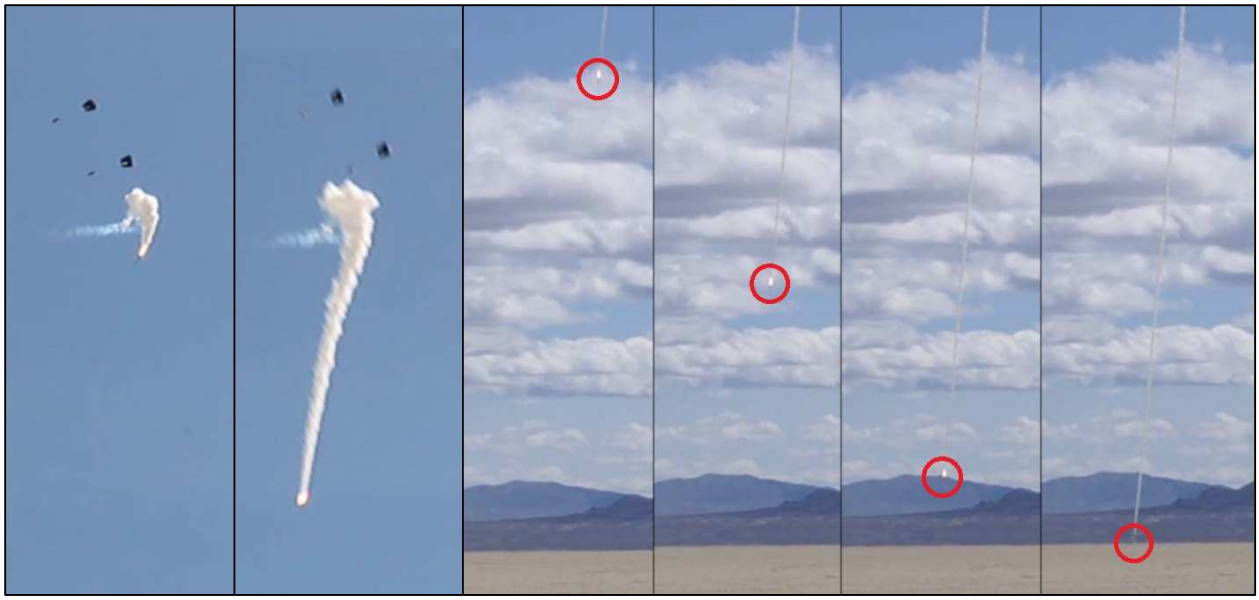

Figure 3.3. Gravedigger 2 was lifted to launch altitude by two power sled kites then used the motor ignition to instantly sever its connection to the kites, reaching an impact velocity of ~420 m/s [30].

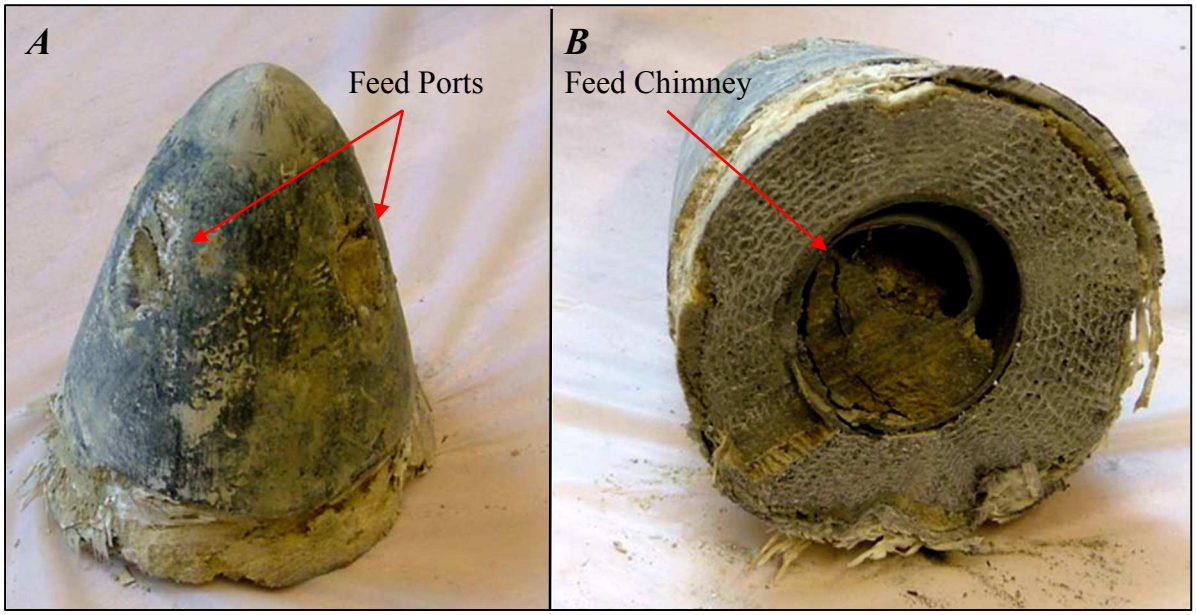

Figure 3.4. While much of the penetrator did not survive the impact, Gravedigger 2's nose cone successfully demonstrated the concept of the collection of material via the feed ports. (*A*) Carbon fiber covered feed ports opened during impact, allowing material to flow into the feed chimney; (*B*) when the nose cone was dissected, ejecta was firmly packed inside the feed chimney where the only available path was through the feed ports.

3.2 IONE, CA: SERIES 1

To eliminate the stage separation problems experienced in earlier test, the rocket was reconfigured to incorporate the second stage directly into the penetrator's airframe, as seen in Figure 2.14. Advances in fabrication techniques allowed for the use of smaller (54 mm diameter), clustered motors that were easier to ignite than the larger (98 mm diameter) motors used in earlier tests. Synchronous ignition of motors in both the boost stage and penetrators proved challenging so during the first series in Ione, testing emphasis was placed on refining the clustered motor methods with a newly developed, student-built flight computer.

The first flight was designed to test both the clustered boost stage's capability, and the post-apogee separation required for a fully powered test where the penetrator's airframe would also be equipped with clustered motors to maximize impact velocity. During the launch, two of the four motors in the boost stage failed to ignite; however, the failed ignition was symmetric, allowing a clean launch but resulting in a lower apogee than anticipated. The new flight computer also failed to separate the boost stage, but despite the anomalies the penetrator embedded nearly normal to the surface with an impact velocity of ~200 m/s. The target material consisted of about 0.61 meters of packed soil, overlying a variety of river stones deposited by a near-by stream that had migrated west over the span of time.

Post-recovery analysis of the penetrator revealed the steel nose cone sustained no significant damage during impact, but sample collection did not occur as hoped. Upon examination, the flow of incoming material appeared to stagnate roughly 0.33 meters after entering the feed port (Figure 3.5). During the impact, sample material becomes compressed by the impact pressure until its failure threshold is exceeded, at which point it behaves in a fluid-like manner; however, as the depth of penetration increases, velocity and pressure decrease and the

initial compaction relaxes and the material behaves more elastically, expanding inside the feed chimney. This behavior was also observed following the analysis of the third penetrator of the campaign, even with different feed port geometry (Figure 3.6). Fine grained material did manage to reach the SRC and was captured by the backflow baffle, but the yield was only around 2 grams.

Figure 3.5. (*A* & *B*) The center-bored feed port, steel nose cone sustained no significant damage; (*C*) measurements made through the aft of the penetrator suggested material flow had stagnated around 0.33 meters after impact; (*D*) the penetrator in cross-section, showing the stagnated material inside the feed chimney; (*E*) close-up of the stagnation point with remnants of the feed port cover (pink shell fragments) mixed in the ejecta.

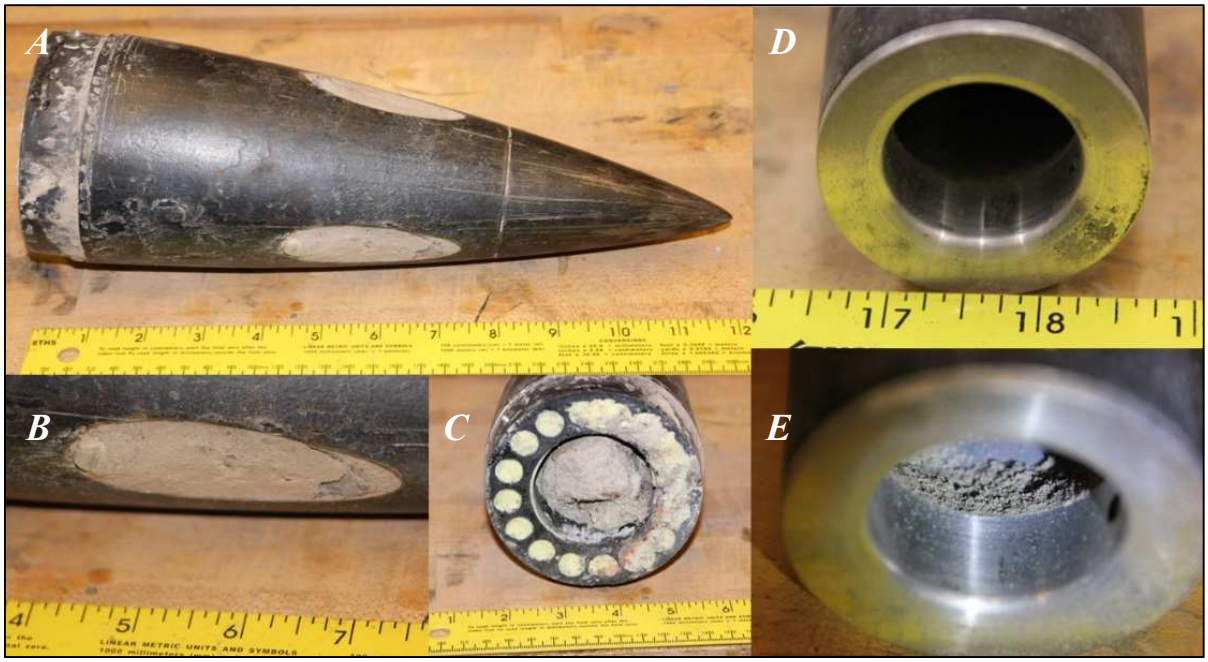

Figure 3.6. (*A*) The nose cone experienced no deformation during impact, (*B*) and feed ports opened successfully. (*C*) Ejecta experienced stagnation at the start of the feed chimney; (*D*) the backflow baffle inside the SRC successfully collected fine ejecta (*E*) that traveled through the feed chimney.

The final flight of the campaign experienced no ignition anomalies, successfully demonstrating the clustered, two-stage flight concept (Figure 3.7). The flight also demonstrated the importance of having a nose cone that is harder than the target material. Impact velocity was estimated to be ~450 m/s, and the penetrator embedded to a depth of ~0.9 meters, having encountered a softball-sized piece of quartzite. The impact deflected the aluminum nose cone, resulting in the penetrator taking a cork-screw like path (Figure 3.8). Additional stresses during recovery separated the crumple zone material along a seam just forward of the SRC. While the SRC survived intact, the twisting of the rest of the penetrator prevented sample material from traveling up the feed chimney.

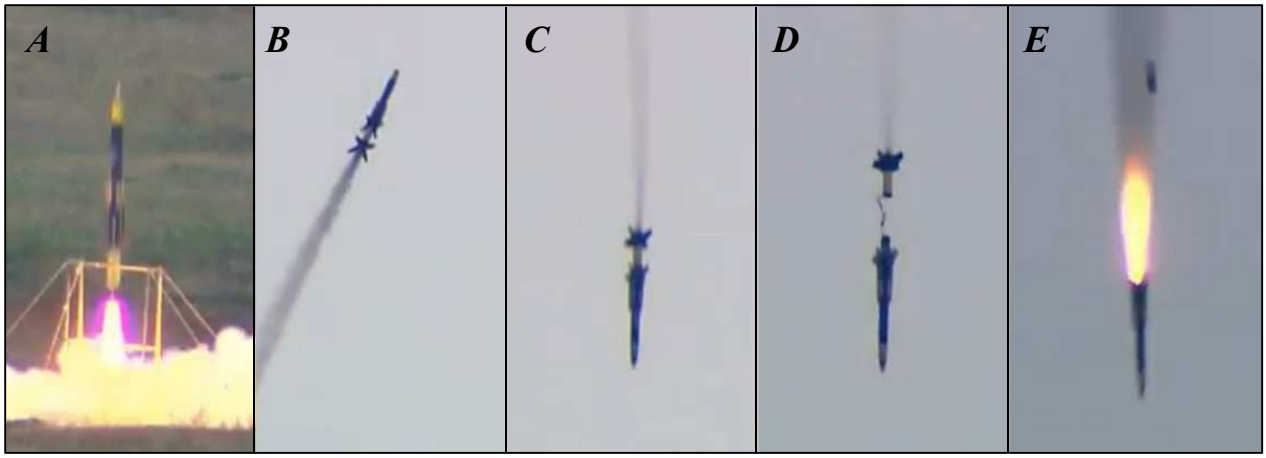

Figure 3.7. (*A*) Successful ignition and launch of the clustered, two-stage penetrator; (*B*) burn-out of the clustered boost stage as the rocket cruises to apogee; (*C*) post-apogee free fall, allowing the rocket to reach aerodynamic stability before igniting the second stage; (*D*) separation of the boost stage; (*E*) ignition of the second stage showing the separation of the inter-stage coupler, containing the flight computer, that was fitted with blast plates to facilitate separation upon ignition of the second stage.

Figure 3.8. (*A*) The penetrator embedded to a depth of ~0.9 meters, but was deflected off a straight trajectory when it struck a piece of quartzite; (*B*) the deflection resulted in massive deformation of the penetrator that separated the body at unreinforced seams in the energy absorbing core material, and prevented sample material from reaching the SRC; (*C*) the aluminum nose cone experienced some deformation during the impact, although the feed ports remained open; (*D*) the contact point where the nose cone encountered the quartzite; (*E*) the SRC remained intact, but warping in the airframe resulted in binding.

3.3 IONE, CA: SERIES 2

The second campaign of penetrator tests outside Ione took place at the end of March, 2015, and while commercial motor issues continued to cause complications, the series resulted in the highest velocity impact to date. Drawing lessons learned during the first Ione campaign, the nose cone was redesigned in an effort to mitigate the stagnation issues found with earlier iterations. Combining the feed port configurations – three, off-set feed ports, and a large, single, concentric feed port – in a new hardened steel tip increased internal flow velocities,

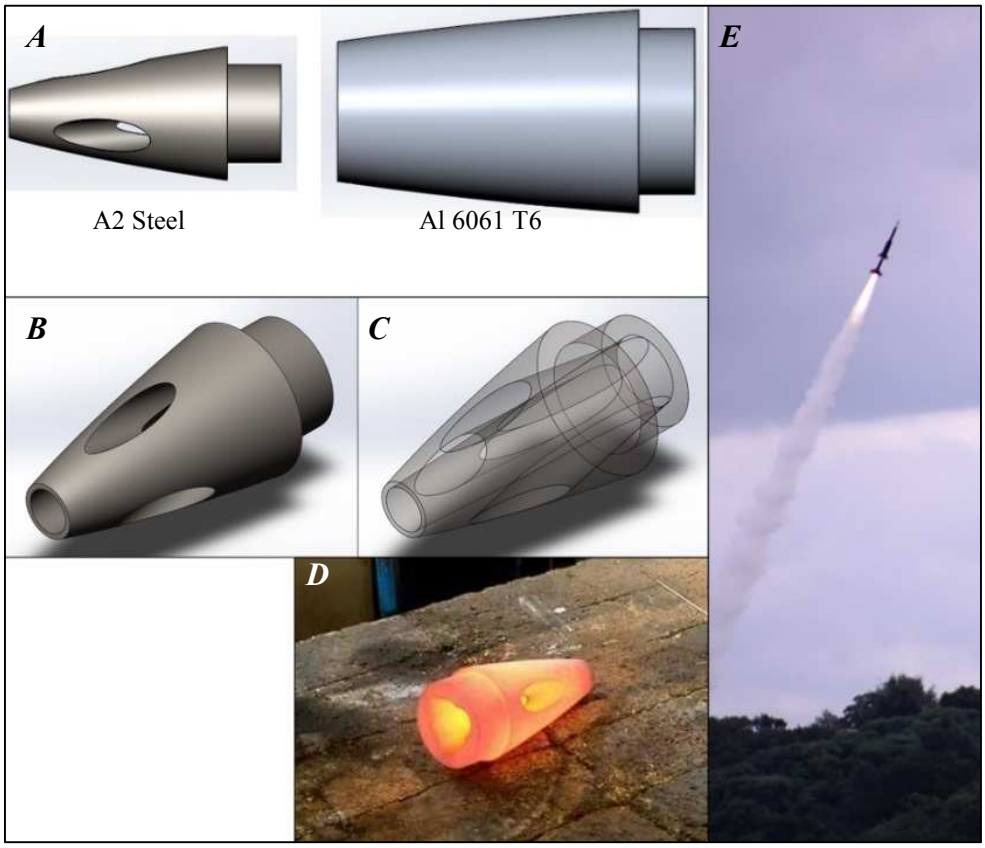

Figure 3.9. (*A*) The steel and aluminum components of the third evolution of penetrating nose cones; (*B*) the hybrid steel nose cone exterior; (*C*) transparent view of the hybrid design showing the confluence of the four feed ports; (*D*) the steel tip after initial heat treating; (*E*) the penetrator equipped with the hybrid nose cone accelerating toward apogee.

while mating the tip to an aluminum extension resulted in an assembly with a mass similar to earlier evolutions. The penetrator was fitted with a full array of eight, outboard motors to provide the highest impact velocity following the post-apogee free fall, and a clustered boost stage was selected for launch after discovering critical components for a large single motor boost stage had not been included with the fuel grains. Slight ignition timing delays in the boost stage resulted in a launch angle of ~30°, reducing the ideal apogee altitude to ~900 meters. While this reduced the planned free fall time, the rocket remained stable during the ignition of the second stage and produced a very loud sonic boom, immediately followed by the sound of the impact. Impact velocity was estimated to be over 600 m/s, embedding to a depth of 1.6 meters into solid sandstone.

The impact was very energetic, and debris from the penetrator was spread across a broad swath of the hillside (Figure 3.10). The impact crater showed less surface disruption than observed in other tests, and only a limited ejecta fan. Once the top few centimeters of soil were removed, the underlying sandstone was revealed and the impact shaft contained a large amount of backfill. Loose backfill debris was removed revealing the top of the impact shaft, ~10 cm in diameter, with clearly observable slickensides (Figure 3.11). Recovery of the penetrator took more than a total of 10 hours, with crew members carving out shoe-box size blocks of sandstone with hand tools. Earlier impact models suggested that material proximal to the impact shaft would experience varying levels of fracturing; however, observations made during the excavation of the penetrator did not validate the predicted response. Instead, the rocket created a shaft with a diameter that matched the maximum diameter of the metal portions of the nose cone assembly of 10.16 cm (where as the main body of the penetrator had a 15.24 cm diameter), with no observable fracturing of material adjacent to the shaft. There was some fracturing and

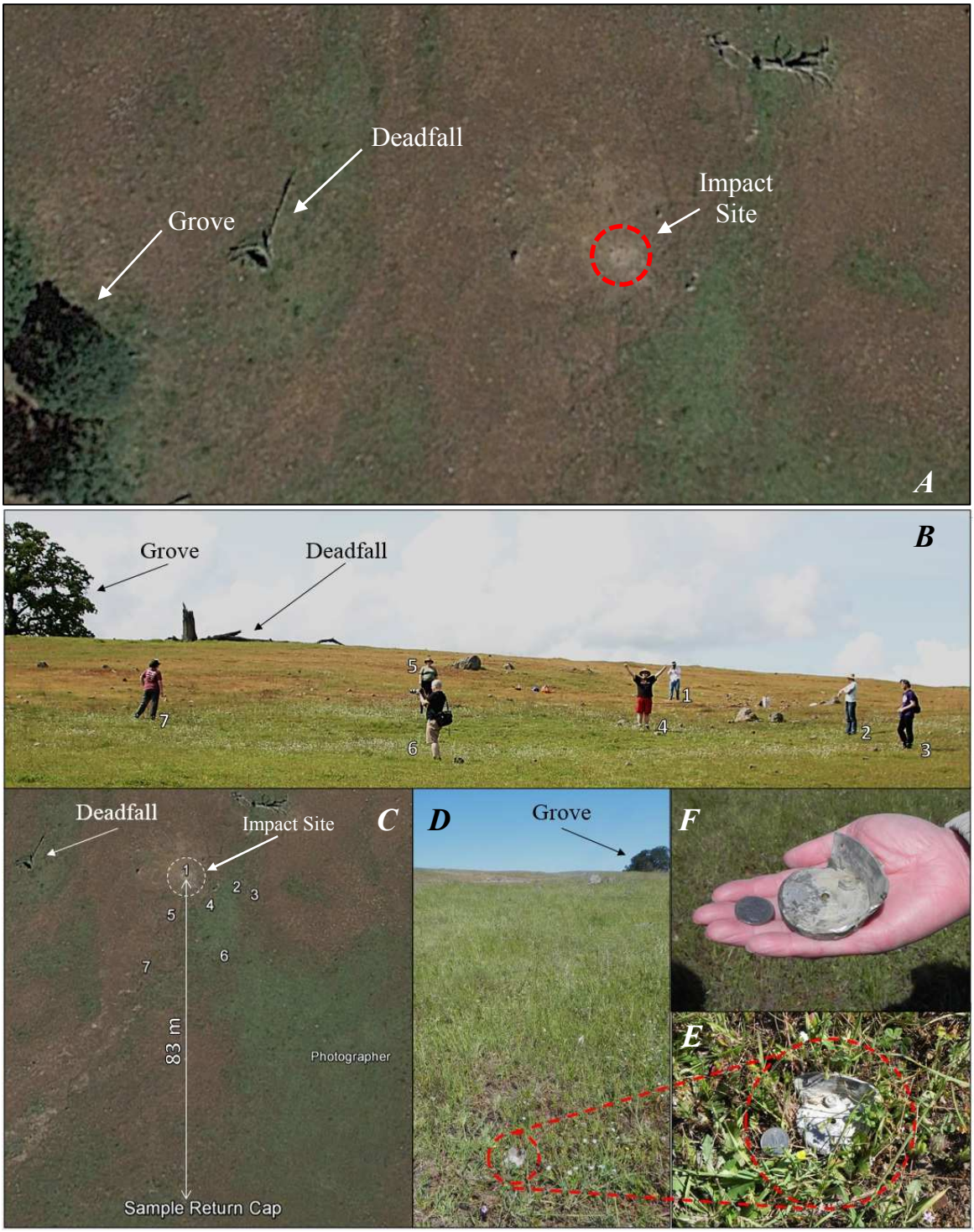

Figure 3.10. (*A*) A Google Earth view of the impact area taken just a few weeks after testing; (*B*)students and researchers stand next to pieces of debris larger than six inches – mainly sheared motor tubes - where numbers reference positions; (*C*) the approximate positions of researchers and students marking major debris, some of which fell more than 80 meters from the impact site; (*D*)(*E*)(*F*) the Sample Return Cap was ejected during the impact.

examples of overturned strata near the surface of the impact site, but these effects were limited to the first few centimeters and were not observed at greater depths. This was an unexpected result, and one that generated behavior in the materials of the penetrator that had not been anticipated by any of the previous models or penetration tests.

Figure 3.11. (*A*) The surface of the impact site exhibited a limited ejecta fan (less than 1.8 X 1.8 meters), with some material overturn, and fracturing of the sandstone around the impact shaft isolated to the top few cm near the surface where confining pressures were the lowest; (*B*) backfill debris filling the 10 cm diameter impact shaft highlighted in red; (*C*) once backfill was removed, slickensides indicative of penetrator embedding aligned along the impacting vector; (*D*) recovery crews spent more than ten hours removing blocks of sandstone with hand tools, excavating to a depth of 1.6 meters.

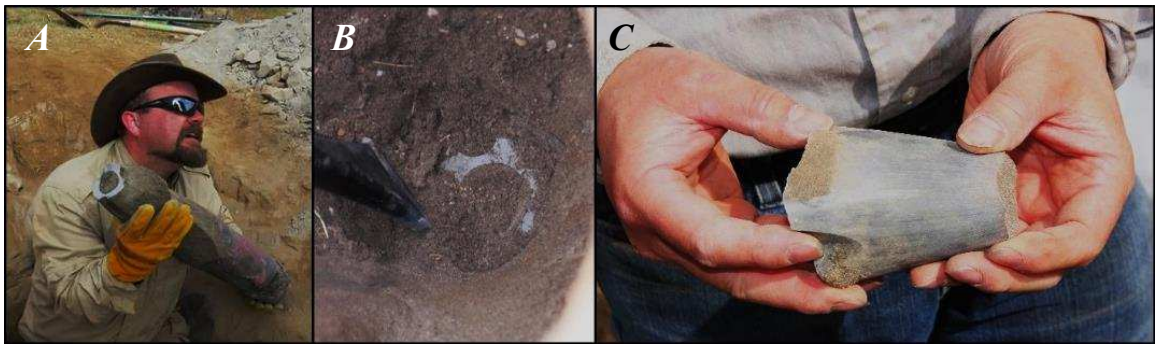

Figure 3.12. (*A*) The removal of the main body of the penetrator; (*B*) forces during the impact resulted in a brittle failure 7.6 cm aft of the front of the steel tip, leaving the separated portion embedded in the sandstone after the main body of the penetrator was recovered; (*C*) the recovered steel tip.

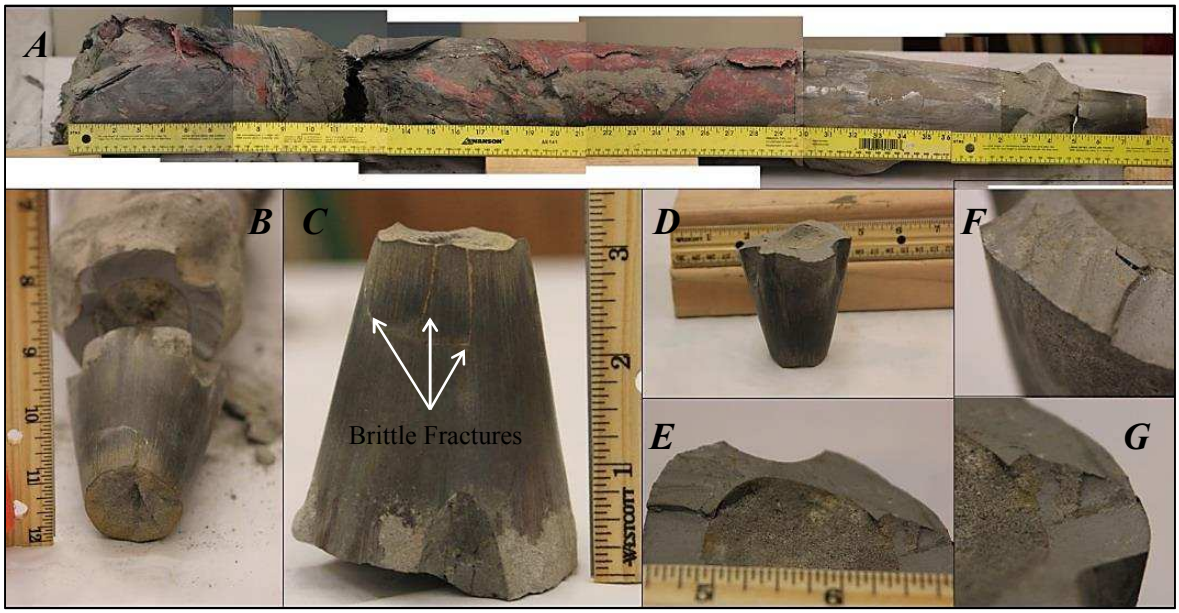

Figure 3.13. (*A*) Composite images showing the recovered penetrator – note the large fracture 0.3 m from the aft of the penetrator and the increasing diameter of the body; (*B*) the steel tip fractured about 7.6 cm from the forward end but the fracture plane exhibited no evidence of impact material coming between the separated portions, suggesting the failure occurred either at the very end of the impact, or only separated from the main nose cone during recovery; (*C*) the front of the center feed port experienced some brittle fractures where the wall thickness was very thin (<4 mm); (*D*)(*E*)(*F*)(*G*) it was initially suspected that the failure plane had originated at the three, off-set feed ports since the wall thickness at those locations was only ~6 mm, however the major brittle failure features occur where wall thickness was ~13 mm.

The diameter of the main body of the penetrator was 15.24 cm, whereas the maximum diameter of the aluminum and steel nose cone assembly was 10.16 cm. Earlier modeling suggested that during embedding, material immediately proximal to the impact would experience significant fracturing during the impact, and in earlier tests into playa and soil there were observed stress fractures that had been created by the impact. The sandstone did not exhibit this behavior however, with proximal fracturing only observed near the surface where confining pressures from the surrounding rock were low. Characterizing the hardness of sedimentary rocks can be challenging and highly dependent on their mineral composition, control samples have not been subjected to tri-axial compression tests so no quantitative values can be assigned to the sandstone; however, it is sufficient to recognize that the strength of the steel and aluminum nose cone was sufficient to penetrate through the formation, while the airframe and energy absorbing materials were not as resilient.

Since the adjoining sandstone did not fracture during the impact as predicted, the metal nose cone assembly bored an impact shaft 10 cm in diameter – the maximum diameter of the assembly. As the 15.24 cm diameter body embedded behind the metal nose cone assembly, the carbon fiber experienced spiral fracturing and was compressed laterally within the confines of the impact shaft. Simultaneously, sandstone collected through the feed ports traversed up the feed chimney to the SRC at a high velocity, creating large internal pressures on the inner diameter of the energy absorbing material. Bound between high external and internal pressures, the honeycombed aluminum and carbon fiber material became compressed into a near solid mass, and was unable to compress along the intended longitudinal direction (Figure 3.14). This compressive behavior was consistent through the initial 0.5 m of crumple zone, but then the material behavior changed.

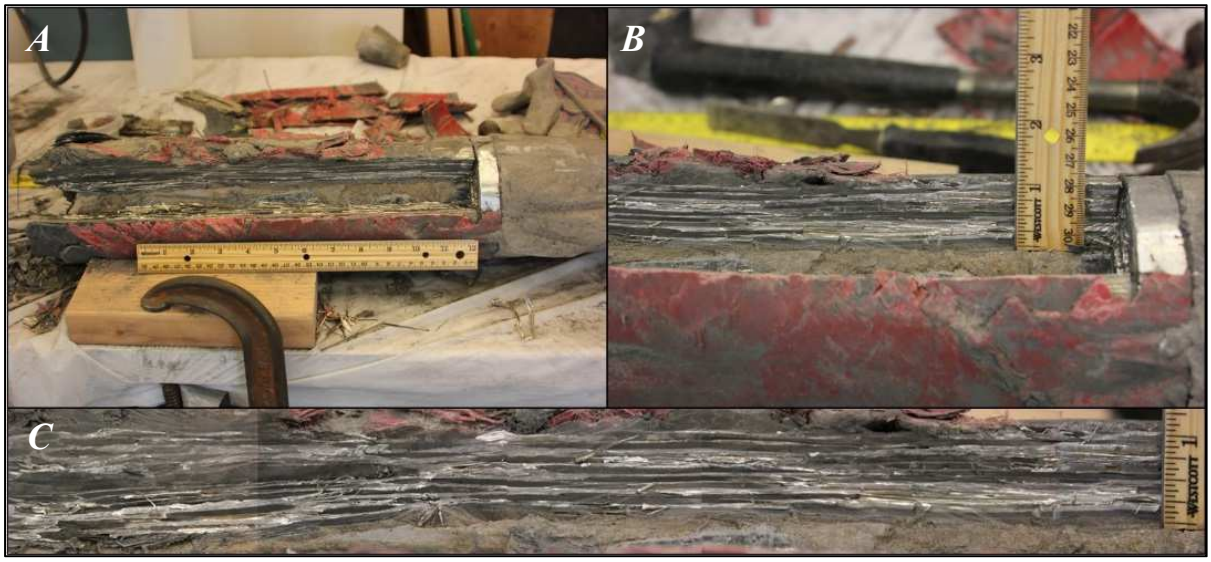

Figure 3.14. (*A*) The initial section of energy absorbing material compressed laterally instead of longitudinally, revealed after the first quarter of material had been dissected; (*B*) the 15.24 cm body diameter compressed to match the 10.16 cm diameter of the nose cone; (*C*) the energy absorbing material, consisting of honeycombed aluminum and carbon fiber rods, became a solid mass. Interestingly, while the aluminum cells had collapsed, the majority of the carbon fiber rods were found to be nearly intact even after the compression.

Serious deformation began to occur after the initial section of crumple zone compression. While spiral fracturing continued up the exterior of the carbon fiber airframe, the section no longer continued to conform to the 10.16 cm diameter of the penetrator ahead of it. Over the length of the 0.3 m of the section containing the SRC, the diameter tapered up to 12.7 cm, and when the outer layers of material were removed, severe deformation in the energy absorbing material and buckling of the SRC was observed (Figure 3.15). The section was then cut in half, revealing the extent of deformation experienced by the SRC. During the impact, sample material flowed at high velocity to about half the length of the SRC, but the pressures created caused the backflow baffle to turn 90˚ inside the SRC. Without the internal pressure of material countering the exterior confining pressure, the SRC buckled and collapsed; the failure occurred after sample

material had entered the SRC, evidenced by the presence of sandstone beyond areas of severe deformation. Forces at work in the SRC resulted in the Sample Return Cap being ejected from the penetrator, coming to rest about 83 meters from the impact site (Figure 3.10).

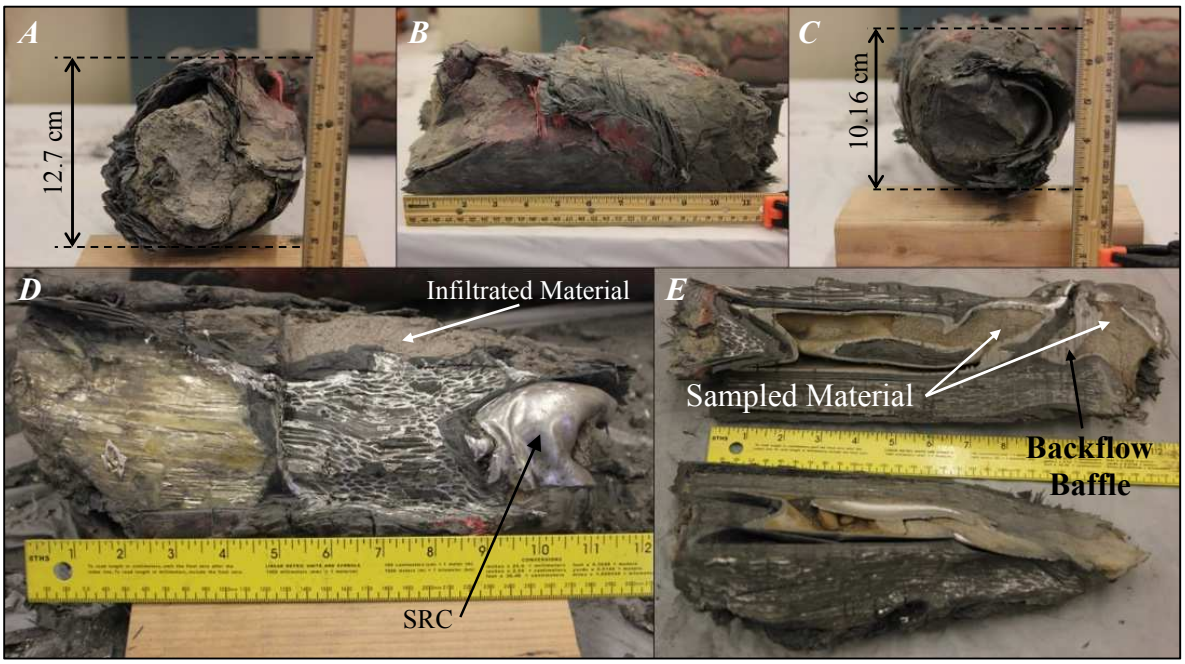

Figure 3.15. (*A*) The aft end of the crumple zone containing the SRC tapered up to a 12.7 cm diameter; (*B*) a side view of the section showing the increasing diameter; (*C*) the forward end of the section that began with a 10.16 cm diameter; (*D*) side view of the section following the removal of exterior layers, showing massive deformation in the honeycombed aluminum, buckling of the SRC, and material that had breached the exterior of the section and did not come from inside the feed chimney; (*E*) when the section was cut in half, the full extent of deformation experienced by the SRC can be observed, showing sample material reaching nearly half the length of the SRC, and the backflow baffle dislodged and turned 90˚.

Regardless of the unexpected material behavior, the test embedded into the hardest material yet sampled by the system, at the highest impact velocity achieved, and demonstrated the potential for penetrators employed for sample return missions. The hybrid design of the steel tip prevented the flow stagnation seen in early evolutions, allowing the sample material to reach

Figure 3.16. (*A*) The core sample was exposed after removing the encasing material; (*B*) note the swelling in the sample diameter near the aft end of the core, indicative of increasing pressures occurring forward of the section that experienced severe deformation.

Figure 3.17. (*A*) The feed chimney after the removal of the core sample; (*B*) the sample core was very solid, and required fracturing it in multiple locations to remove it from the chimney; (*C*) sample material in the nose cone was left in place given the difficulty in removing it intact.

the SRC. The energy absorbing material along the length of the constant 10 cm diameter of the penetrator was removed with the adjacent section of carbon fiber feed chimney, revealing the collected core sample (Figure 3.16 and Figure 3.17).

3.4 IONE, CA: SERIES 3

For the final set of field tests, the penetrator was redesigned in an effort to ensure full ejection of the SRC. Aluminum shoulders extended the maximum diameter of the nose cone assembly to match the body of the penetrator and the steel SRC was moved fully forward in the penetrator so that it extended beyond the end of the machined nose cone (Figure 3.18). The SRC was epoxied in place and its feed port was covered for flight (Figure 3.19); the epoxy was sufficiently robust enough to survive flight, but the contact joint would shatter on impact allowing the SRC to move through the penetrator. During the field test motor ignition failures in the second stage resulted in a lower impact velocity than desired that was estimated to be about 330 m/s. Despite the setback, the system performed as expected successfully collecting sample material from depth and ejecting the SRC during the impact.

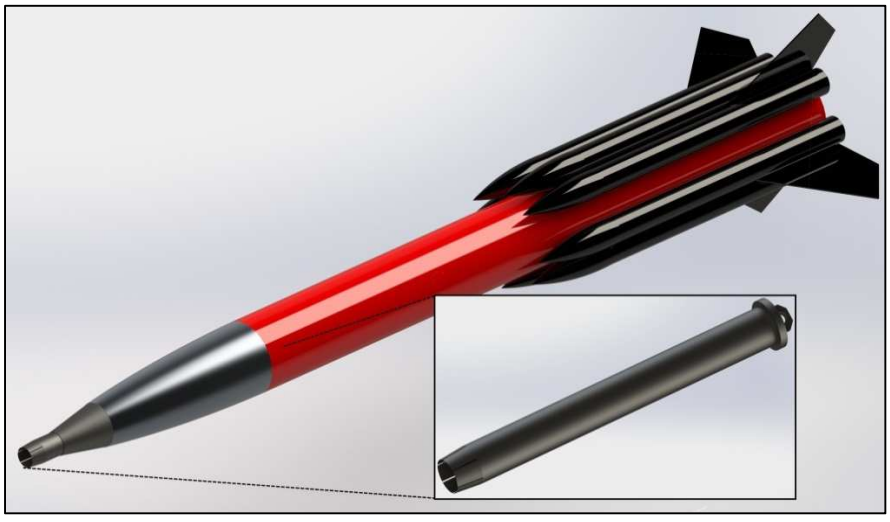

Figure 3.18. The redesigned penetrator moved the SRC fully forward.

Figure 3.19. (*A*) The epoxied SRC with its tip in front of the main nose cone and (*B*) the penetrator system ready for flight.

The penetrator embedded to a depth of about 1.27 m at an angle of about 15˚ off normal to the surface. The impact angle and ground vegetation limited the span of the ejecta fan to about 1.5 X 1.5 m, with the SRC coming to rest about 2 m from the embedded penetrator (Figure 3.20). A frame by frame analysis of a video reveal the SRC being entraining part of the smoke plume as it ejected, with an ejection estimated velocity of ~10 m/s. (figure 3.21). After

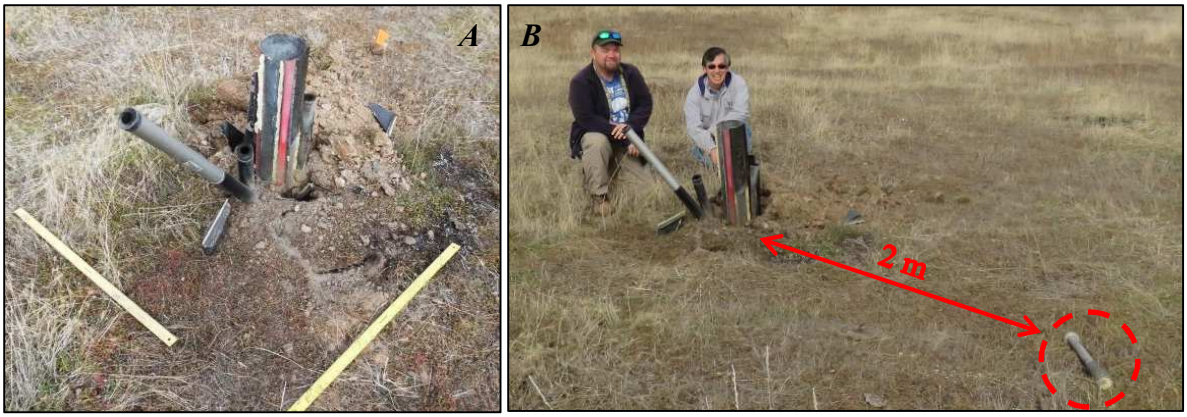

Figure 3.20. (*A*) The impact site showing a limited ejecta fan and (*B*) researchers at the impact with the SRC 2 m away in the foreground.

Figure 3.21. (*A*)(*B*)(*C*)(*D*) Still frames from a video of the impact show the SRC entraining part of the smoke plume as it ejected at about 10 m/s, coming to rest about 2 m from the embedded penetrator. (*E*) The penetrator embedded to a depth of 1.27 m through stratified layers of soil, clay, and talc.

excavation, the impact area was found to consist of about 0.3 m of soil and clay overlying a bed of talc.

The redesigned steel SRC fared much better than earlier aluminum and carbon fiber iterations. The forward end of the SRC had been tapered and slotted in an effort to create a self-closing container with the slotted tabs folding over the feed port during impact. Three out of six tabs successfully folded, with three of the tabs shearing off – largely due to the impact angle – and no deformation along the length of the rest of the SRC was observed (Figure 3.22). The SRC body was cut open, revealing stratified layers of soil, clay and talc (Figure 3.23). A comparison of the stratified sample with the impact site suggest SRC ejection occurred at a depth of about 0.4 m estimated using the 3 cm of talc at the forward end of the sample.

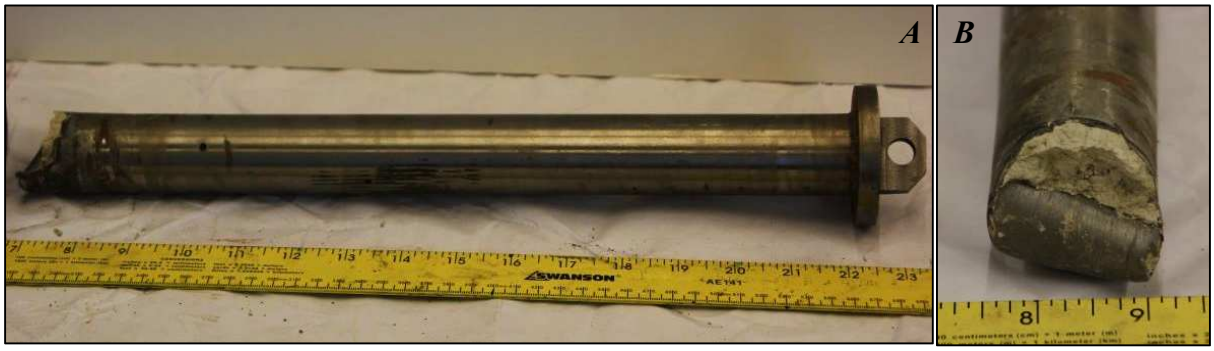

Figure 3.22. (*A*) The recovered SRC showed no deformation along its length and (*B*) slotted tabs at the feed port folded over during impact to partially close the SRC.

Figure 3.23. Opening the SRC revealed the stratification observed at the impact site had largely been preserved during the impact.

Chapter 4. THE POTENTIAL FOR METAMORPHIC EFFECTS

4.1 IMPACT METAMORPHISM

The International Union of Geological Sciences Subcommission of Metamorphic Rocks defines metamorphism as "…a subsolidus process leading to changes in mineralogy and/or texture (for example grain size) and often in chemical composition in a rock...These changes are due to physical and/or chemical conditions that differ from those normally occurring at the surface of planets and in zones of cementation and diagenesis below the surface" [31]. Increasing depths result in rises in pressure and temperature producing a variety of alterations in material, depending on the conditions it is subjected to. Metamorphism can be classified under five major categories: Contact Metamorphism is the result of thermal effects from intruding magma into cooler rocks; Regional Metamorphism is similar to Contact Metamorphism except on scales that make distinguishing individual contacts difficult; Hydrothermal Metamorphism is the result of interactions between minerals and water; Fault-Zone Metamorphism results in high-stress deformation in areas that experience large shear stresses; Impact Metamorphism results from the collision of meteorites and asteroids, or may occur during the explosion of a bolide [32]. Of the five categories, Impact Metamorphism differs the most in the higher temperatures and pressures created, as well as in the much shorter time-scales in which the alterations occur. Figure 4.1 shows pressure and temperature plots for various metamorphic facies that occur in Earth's lithosphere, as well as pressures and temperatures that occur during impacts.

SaRSEE impact velocities are well below the hyper-velocities that occur during meteorite impacts, but the small contact areas forward of the feed ports have the potential to create pressures that could affect sampled mineralogy. An understanding of these pressures can be

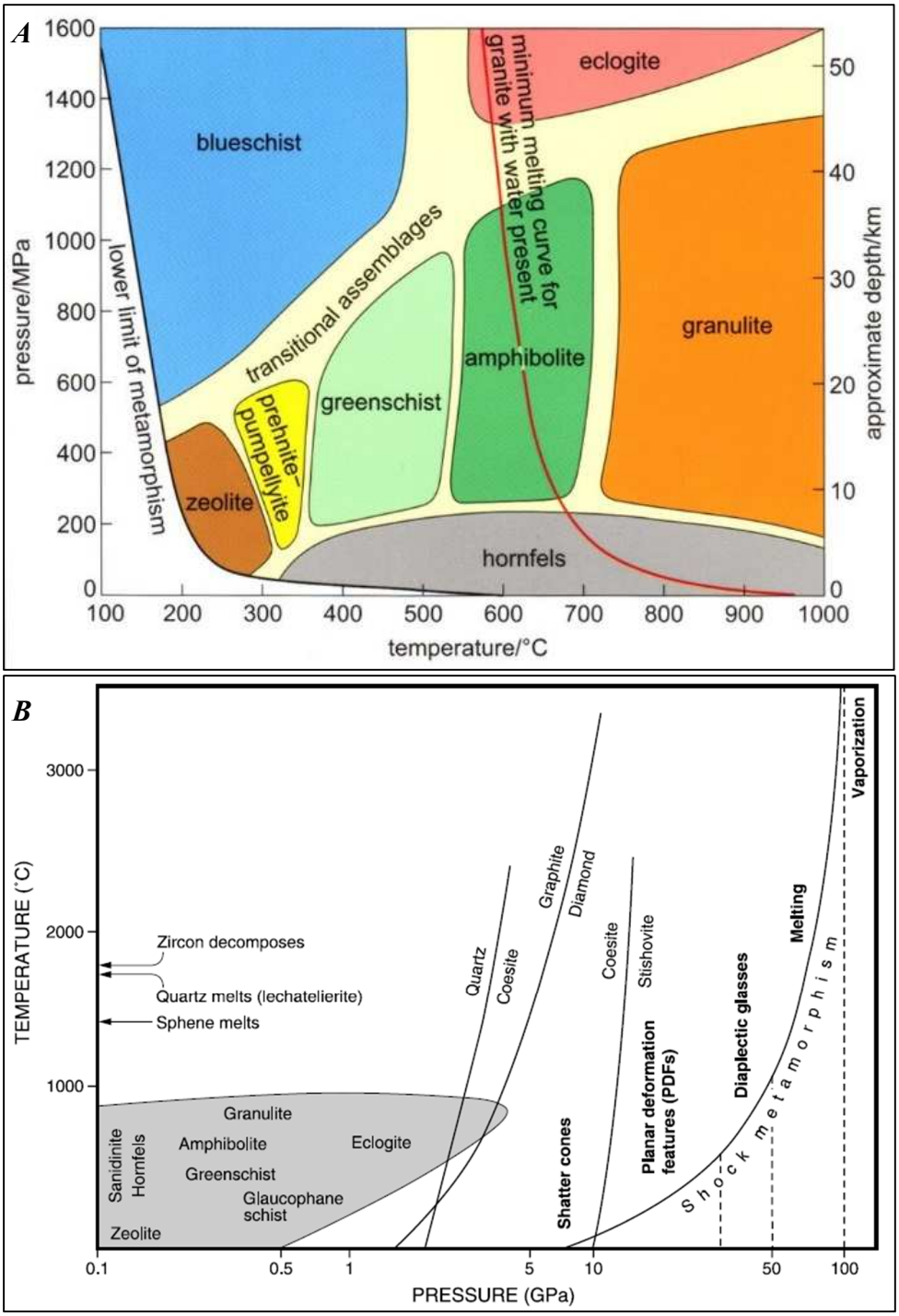

Figure 4.1. (*A*) Plot showing the metamorphic facies that occur at given pressures and temperatures, corresponding to the depths that these conditions exist at in the lithosphere, with pressure (in MPa) and depth shown on the vertical axis [33]; (*B*) plot showing temperatures and pressures generated during impact, with pressure (in GPa) shown on the horizontal axis, where the grey area corresponds to the temperature and pressure ranges shown in (*A*) [34].

used to provide an acceptable impact velocity that limits these effects, and assists in selecting primitive bodies where impact sampling might be employed.

4.2 Impact Velocity and Pressure

Efforts at creating predictive equations for penetration depth have been ongoing since the mid-eighteenth century as engineers sought insight into designing more robust earth-works for defending against artillery bombardment. Newton's equation for motion was used as a foundation for beginning the estimates, but it quickly became clear that most naturally occurring materials lacked the homogeneity required and that multiple functions were necessary to incorporate more realistic material behaviors [35]. In the second half of the twentieth century, an empirical approach was investigated by Sandia Laboratory, and the resulting equation has proven to be reasonably accurate for predicting earth penetration depth, and subsequently impact velocity. The impact into sandstone during the second flight series in Ione (see section 3.3) was the highest velocity impact into the hardest target material out of all the tests, and as such produced the most extreme conditions during embedding. In order to hypothesize about the pressure created during that test, an impact velocity estimate can be calculated through the application of Young's Empirical Equation for penetration depth [36]:

$$D = \alpha K_s S N \left(\frac{m}{A}\right)^{0.7} (V_s - 30.5) \tag{4.1}$$

rewritten for impact velocity becomes:

$$\boldsymbol{V_s = \frac{D}{\alpha K_s S N \left(\frac{m}{A}\right)^{0.7}} + 30.5} \tag{4.2}$$

where the variables represent:

$$penetration\ depth \rightarrow D = 1.5748\ meters$$

$$angle\ of\ attack\ \rightarrow\ \alpha = 0.0000175$$

$$scaling\ factor\ for\ rock \rightarrow K_s = 0.46(m)^{0.15} = 0.7343$$

$$empirical\ constant\ for\ sandstone \rightarrow S = 0.76\ to 1.30$$

$$penetrator\ nose\ coefficient \rightarrow N = 0.18\left(\frac{L_n}{d}\right) + 0.56 = 1.4366$$

$$metal\ nose\ cone\ length \rightarrow L_n = 0.2333\ meters$$

$$penetrator\ diameter \rightarrow d = 0.1565\ meters$$

$$penetrator\ mass \rightarrow m = 22.6\ kg$$

$$penetrator\ cross-sectional\ area \rightarrow A = 0.01923\ m^2$$

$$impact\ velocity \rightarrow V_s$$

The sandstone impacted has not been empirically tested to determine its cohesive strength, saturation, viscosity, and other natural variations in rock and soil that can vary widely depending on the particular formation [35]. Values for S, the constant in Young's equation for characterizing the impacted material, were sourced from the National Research Council report [36] but the published values were problematic since S is an empirically determined constant, and the published values provided quantify 0.76 for medium-strength rock, and 1.30 for low-strength rock. As such it was helpful to look at a range of values for S to dial in the impact velocity estimate based on the observed penetration depth. Flight simulations indicated a maximum impact velocity of 686 m/s, but this velocity assumes ideal aerodynamic drag which the rapid fabrication methods employed could not achieve. A reasonable upper limit for the maximum velocity achieved is estimated to be around 640 m/s; many of the recovered motor tubes contained remnants of unburned fuel grains that suggest complete burn out had not occurred at the time of impact, indicating the rocket was still accelerating at impact and making 640 m/s a reasonable upper limit. Flight simulations for an earlier, heavier evolution predicted a

maximum velocity of 580 m/s, so this was selected for a lower boundary. Values of S were increased by increments of 0.1, and the resulting estimate shows only one value of S falling within the upper and lower limits shown in Figure 4.2. It is important to note that this is only an estimate of the actual impact velocity, but the 630 m/s prediction is reasonable to the first order.

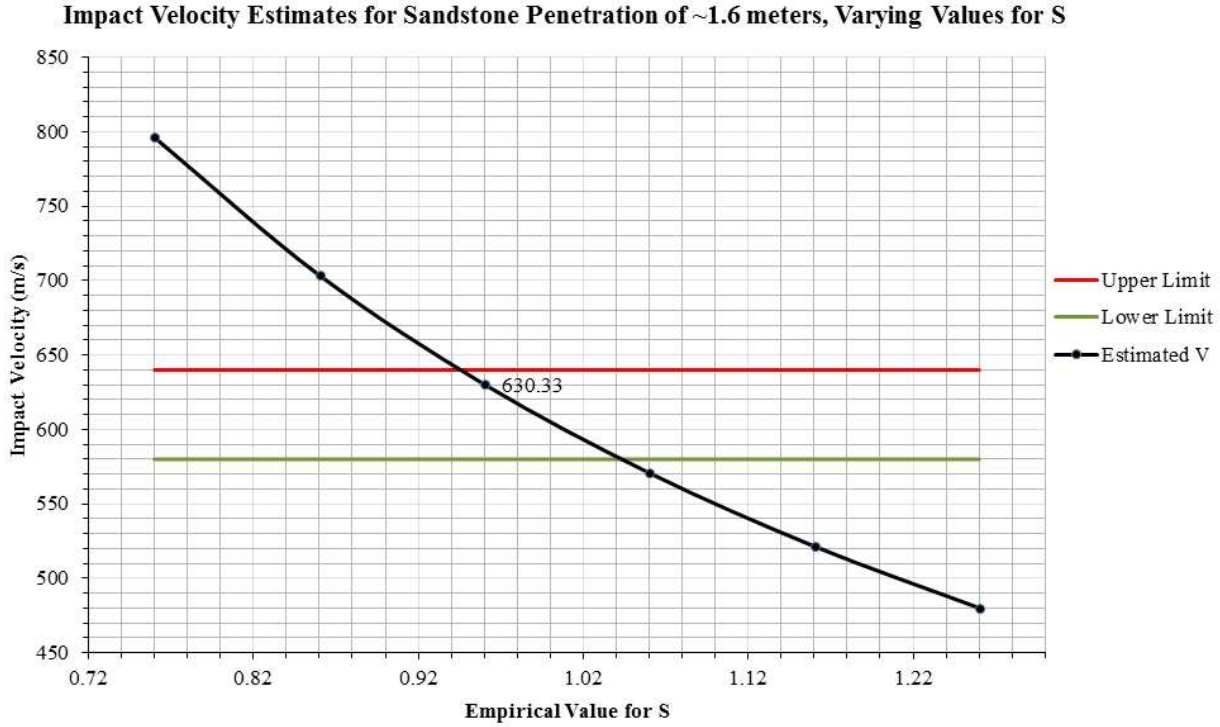

Figure 4.2. Using Young's Empirical Equation, the estimated impact velocity was ~630 m/s.

To the first order, an object impacting at a velocity of 630 m/s and embedding to a depth of 1.6 meters completes the process in about 2.5 milliseconds, corresponding to a deceleration of about 248,063 m/s^2. Therefore, a 22.6 kg penetrator generates about 5.6 MN of force during impact (about 4.5 MJ of kinetic energy). To estimate initial pressures created during the embedding, only the surface area of the steel tip that included the feed ports was used since any alteration of material that occurs after this region is not sampled by the system. With an estimated contact force of 5.6 MN, and a surface area of 0.032 m^2, pressure during the initial embedding is estimated to be 175 MPa; however, since this pressure estimate uses the entire

surface area of the feed port region, the 175 MPa should be considered a lower limit. When the same force is applied at the surface of the center feed port, the smaller contact area of 0.00034 m^2 results in a pressure of about 16.5 GPa. This should be considered the upper limit of a dynamic pressure gradient that occurs across the surface of the nose cone, decreasing as the contact area increases during embedding.

The range of estimated pressures occurring during initial embedding lends little clarity to the potential for metamorphic effects in the sampled material. The extremely short time scales of just a few milliseconds does not allow for normal metamorphism associated with terrestrial processes, while the impact velocity is roughly half of what an average impacting meteorite experiences, to say nothing in regards to the increase in kinetic energy released by a more massive impactor. The rapid embedding also means that thermal effects during the impact are also negligible, even when considering the upper limit of 16.5 GPa since impacts where pressures are under 40 GPa result in post-shock temperature increases of less than 500˚ C which is below the melting point of most rock-forming minerals [34].

4.3 Observed Impact Effects in the Sandstone

The test area outside of Ione, California provided a geologically diverse environment that has been the subject of studies ranging from economic-mineralogic descriptions and paleoclimatic influences, to depositional environments and stratigraphic context to Great Valley units [37]. By combining previous scholarly work with satellite imaging and geologic maps, the specific formation at the impact site was identified allowing for a preliminary identification of the sampled sandstone. Shown in Figure 4.3, the penetrator embedded in a portion of the Valley Springs Formation adjacent to the Sacramento-Amador County line. The Valley Springs sandstone is believed to be the result of fluvial deposition from ancient valleys in the Sierra

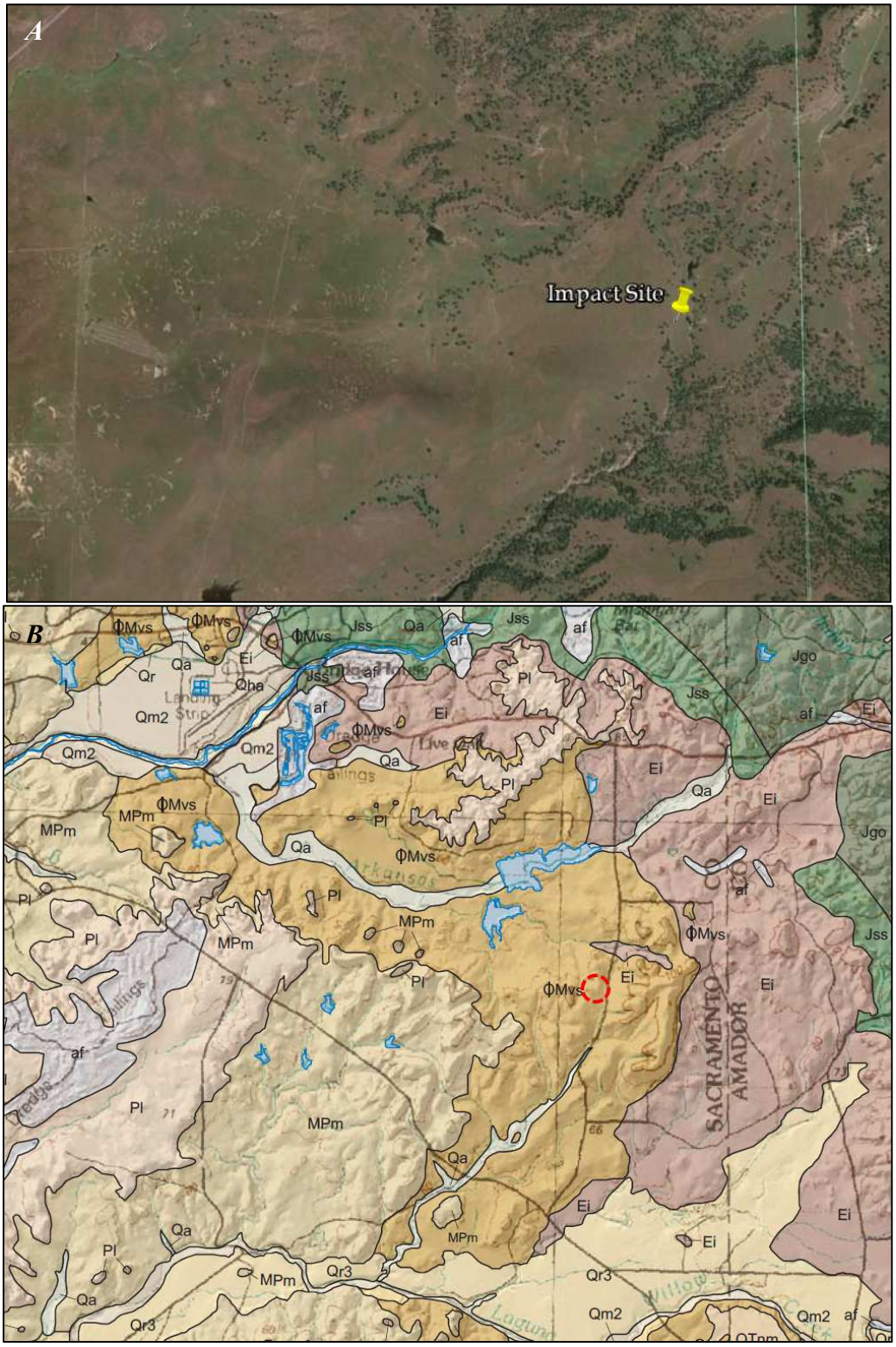

Figure 4.3. (*A*) Google Earth imaging was used to identify the impact site and compared with (*B*) a geologic map of the area to identify the formation that was sampled [38].

Nevada range to the east, can vary in color from white to light grey or tan, has a matrix dominated by kaolinite, and has higher abundances of feldspar, biotite, and lithic grains than sandstones from adjacent formations [37][39].

The high velocity of the impact, and particular geometry of the feed ports used during the test (see section 3.3), resulted in material being collected as a cataclastic flow - the mechanical fragmentation of a rock body – which alters the original orientation of crystals in the mineral assemblage. Additionally, alterations in the mineralogy from shock waves created during embedding should be observable in thin sections created from sampled material; however, thin sections created from the removed core (see section 3.3), as well as thin sections created from sandstone that had not been impacted, proved extremely problematic. The standard impregnating resins normally used proved to be too viscous to adequately permeate the billets, and as such none of the thin sections created survived their final polishing since the materials simply washed away. While photographs of both the control and sample materials under cross polarized light were taken prior to their final polishing, the material was not at the appropriate thickness to allow for proper mineral identification. Limitations of time and resources prevented additional attempts to recreate the thin sections within the framework of this paper.

Despite these shortcomings, a qualitative assessment can be made by examining the photographs of the sections made prior to their destruction. Figure 4.4 shows two of the thin sections slides created, where the dashed boxes highlight regions shown in higher magnification in Figure 4.5. Neither thin sections show a preferred orientation for any of the minerals, suggesting that alterations from cataclastic flow have negligible effects when sampling sedimentary materials. Additionally, the core sample does not exhibit more fracturing of the crystals than seen in the control, although there is a noticeable decrease in the interstitial spaces

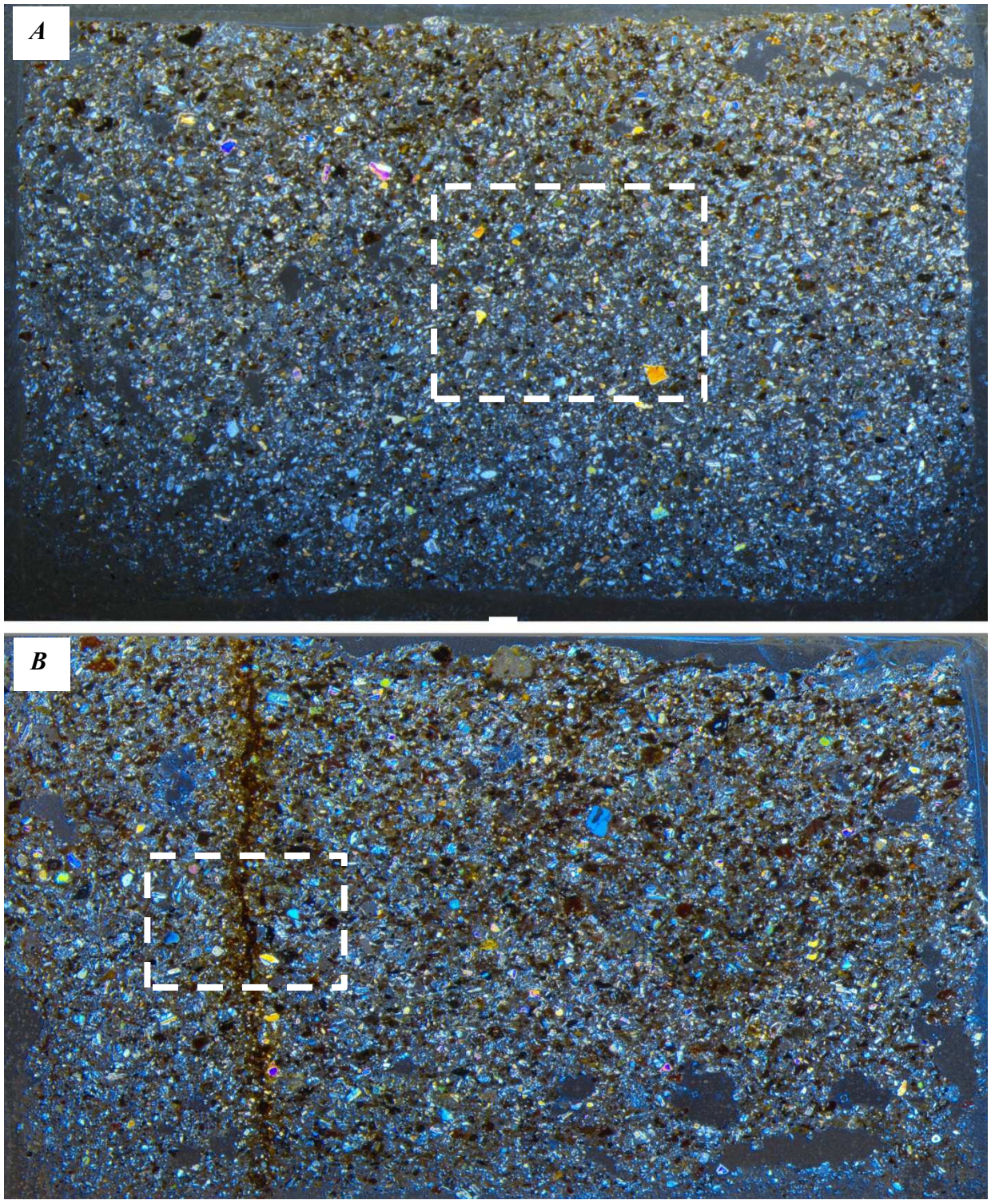

Figure 4.4. (*A*) A thin section created from sandstone from the area of the impact site that was not impacted and (*B*) a thin section created from material taken from the core of sampled material.

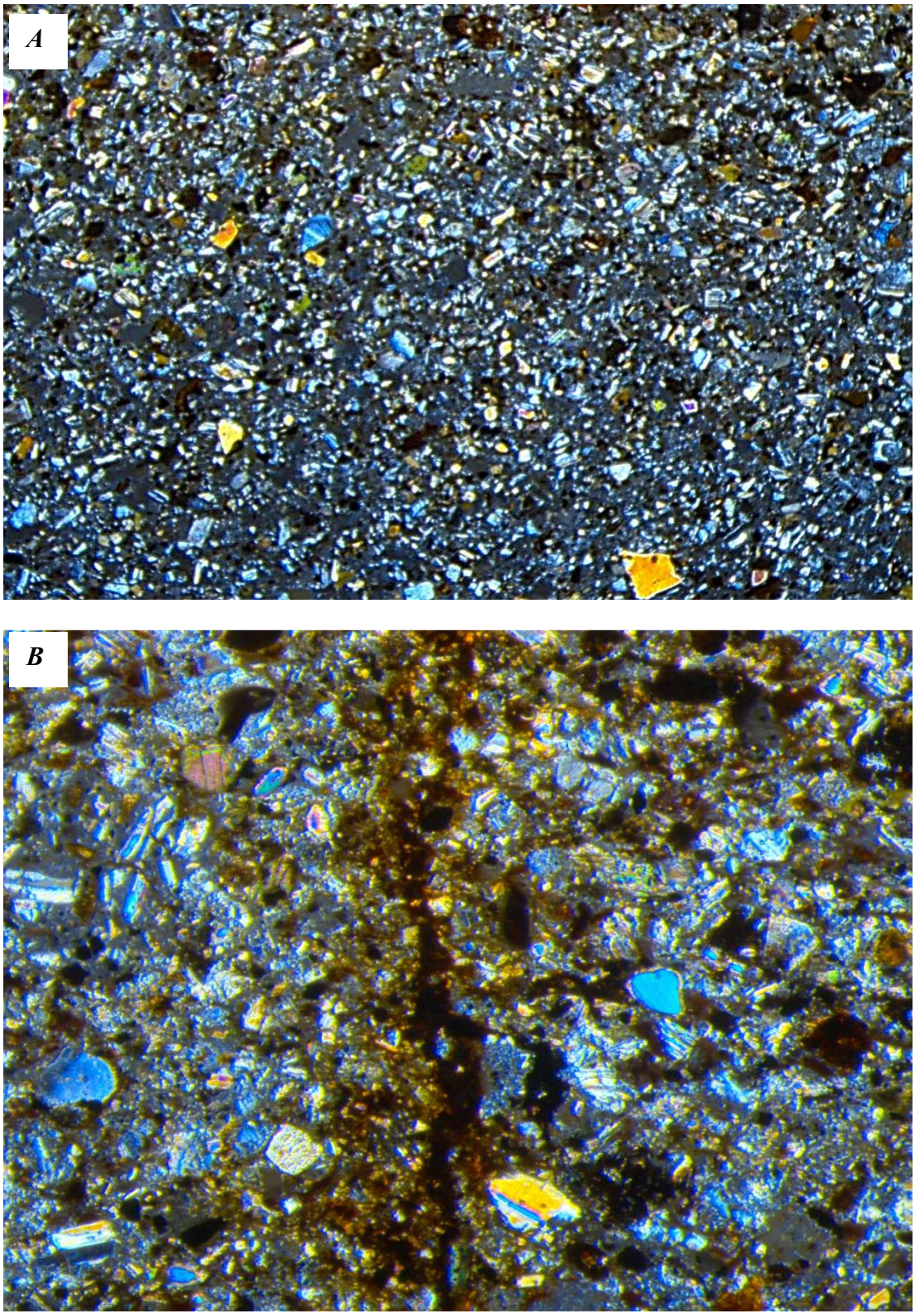

Figure 4.5. (*A*) The control sample under higher magnification, where the dark grey matrix between the crystals is the embedding resin and (*B*) the core sample under higher magnification.

due to the repacking of the material during embedding. This observation is consistent with density measurements taken of both the control sample and the core: the control sample had a measured density of 1.7 g/cm^3; the core sample had a measured density of 2.1 g/cm^3.

The most intriguing feature observed in the core sample was an unusual discontinuity that can be seen running vertically in both Figures 4.4 *B*, and 4.5 *B*. The discontinuity seen in the images is only a section of an orange colored ring that was discovered to run throughout the length of the core sample. Once again, the inability to complete the thin sections prevented a detailed identification of the material, so origins and possible mechanisms of how the ring was created are purely speculative at this time and as such will be addressed in the next chapter. There were no significant differences observable in fracturing of the mineralogy between the control and core samples, nor were there clearly identifiable traces of shock metamorphism, such as kink banding in the mica crystals. This suggests that at similar impact velocities shock metamorphism may not significantly detract from the science value of samples collected from primitive bodies using planetary penetrators.

Chapter 5. DISCUSSION

Results from field tests indicate that the use of penetrators for sample return is in fact feasible, but many questions remain to be answered. While metamorphic effects in the impacted material sampled during testing seem negligible, there are a number of processes that occur during the impact that are poorly understood.

5.1 THE ORANGE RING

As mentioned in section 4.3, once the sample had been removed from the penetrator, an unidentified ring was observed inside the core that ran at a consistent diameter throughout the length of the core. The ring was about 4.5 cm in diameter, and can be seen in figure 5.1.

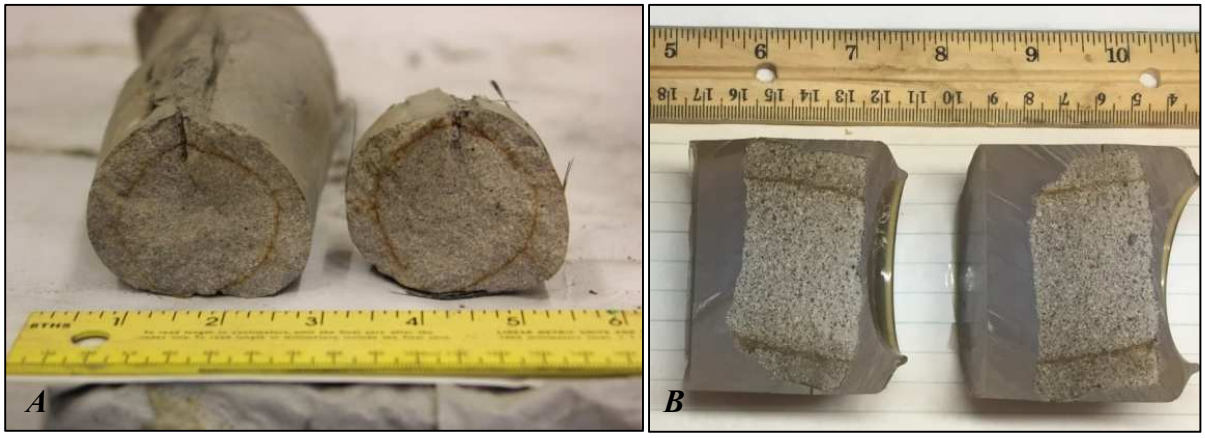

Figure 5.1. *(A)* An orange ring was observed in the sandstone core sample that ran throughout the length of the core. (*B*) Half sections of core material in embedding resin show the ring running through the core parallel to the flow of material.

Difficulties in completing the thin sectioning of the core sample prevented a quantitative analysis of the composition of the ring. A number of hypotheses concerning mechanisms that could have resulted in the formation of the ring have been made such as the migration of highly mobile elements during embedding, or an increased reaction of water and iron naturally

occurring in the formation that rapidly oxidized under the impact pressures; however, neither of these ideas can account for either of these processes occurring during the 2.5 milliseconds of embedding, nor can they account for the nearly perfect concentricity of the ring with the penetrator. The most likely hypothesis is that the ring is the result of scouring away of surface material from the inside of the steel nose cone.

As seen in Figure 3.13, imprecision during the hardening and tempering of the A2 steel tip resulted in brittle fractures during the impact. During embedding, portions of the tip that fractured away would have been entrained with the sample material, and there appears to be a diffused staining of the sample material, shown in Figure 5.2. An examination of the failure plane where the steel tip fractured through revealed additional staining, although the discoloration was no longer diffusive as it was at the tip, but rather appeared more like a stripe that ran across the diameter of the core material. Finally at the aft edge of the core material that was left in place (see section 3.3), the ring can be seen with the 4.5 cm diameter that continued throughout the rest of the core, shown in Figure 5.3.

The most compelling evidence to support the idea that the ring was the result of steel abraded into the flow during embedding is the diameter of the ring itself. At 4.5 cm, the diameter of the ring matches the exit diameter of the steel portion of the nose cone assembly. This may be coincidental however, and ultimately answering this question will require the completion of thin sections of the core material to assess the ring's composition. While the diameters of the ring and exit port of the steel match it does not account for why material that expanded into the feed chimney beyond the ring does not bear the same discoloration, or why in the photographs of the only thin sections attempted why the discontinuity looks more like a melting of the matrix and not the adjacent mineral crystals (see Figure 4.5 *B*).

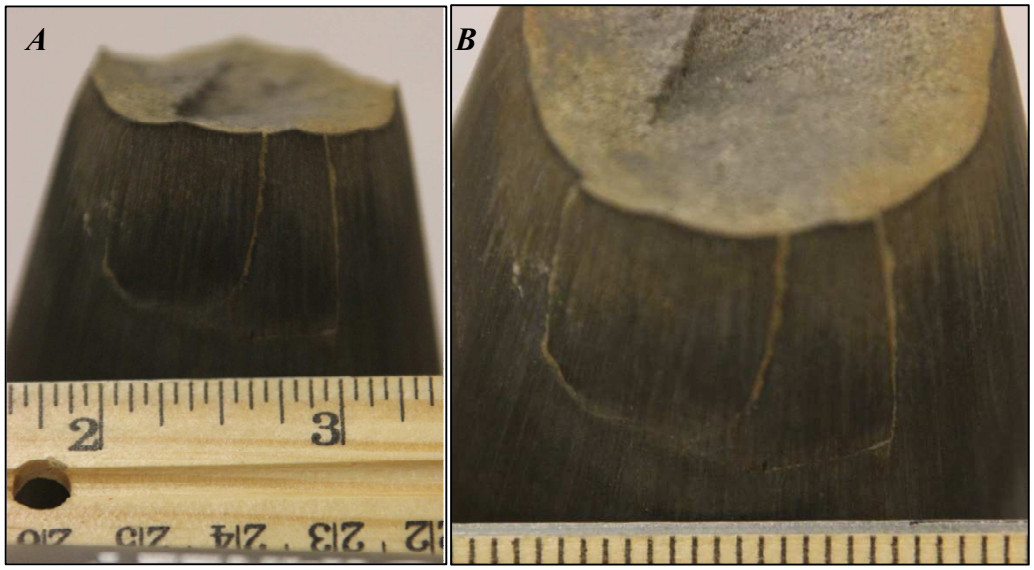

Figure 5.2. (*A*) Material missing from the forward edge of the nose cone would have been entrained with the sample material, and (*B*) staining that appears to diffuse inward from the steel into the sandstone.

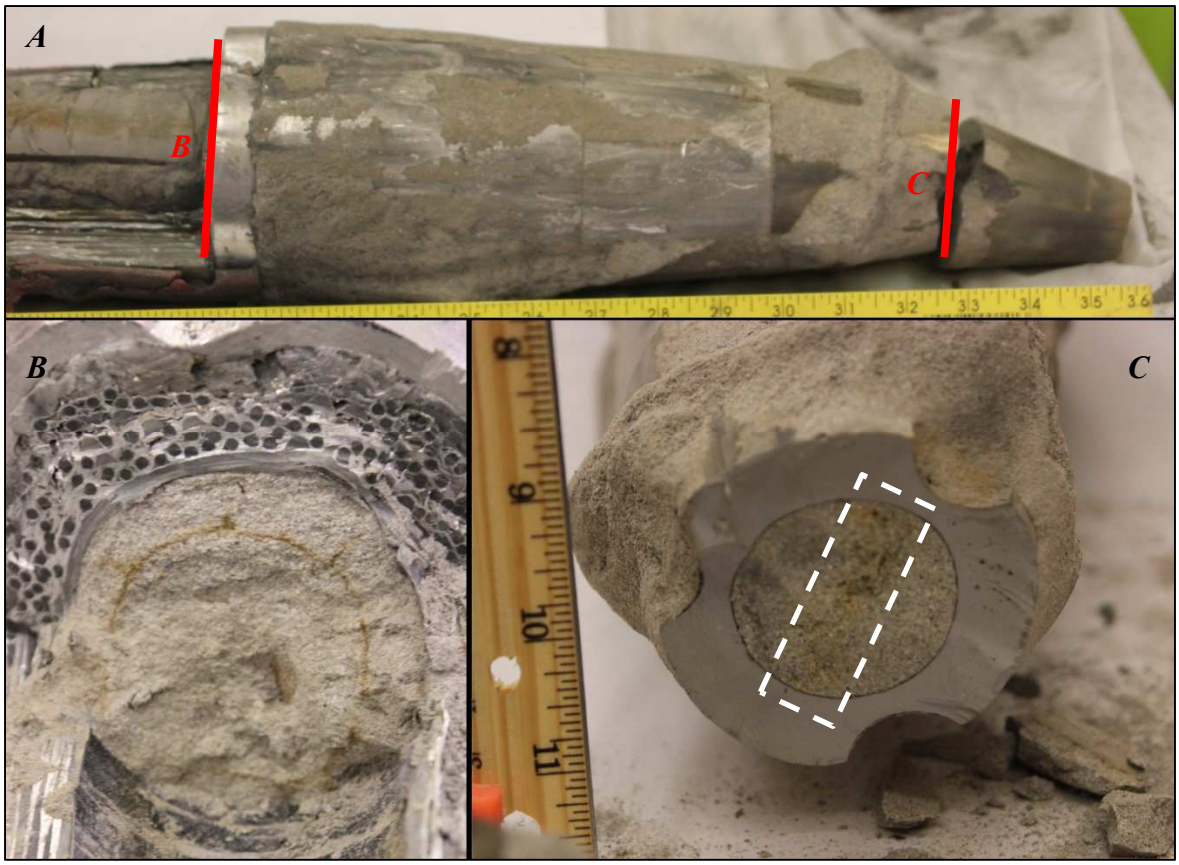

Figure 5.3. (*A*) The nose cone assembly showing the locations of (*B*) the clearly formed ring and (*C*) the discolored stripe.

5.2 Penetration Depth and Sample Ejection

During the fabrication for the final flight series (see section 3.4) the choice was made to move the SRC fully forward in the penetrator assembly in an effort to demonstrate the system's ability to self-eject the sample (see Figure 3.18). While the design change ultimately resulted in the ejection of the SRC, the ejection was estimated to occur at only one third of the depth that the system embedded to and as such the majority of the potential core sampled remains behind with the main body of the penetrator. Similarly if the SRC had ejected during the sandstone shot, only the upper third of the created core would have been ejected.

In the larger view of sample return missions where past efforts have largely retrieved less than a gram of surface material, this may seem insignificant. The sandstone impact described in section 3.3 collected about 3.2 kg of subsurface material, and even the successful return of only a third of that sample would increase the return yield by at least an order of magnitude compared with previous un-manned sample return missions. However, to better understand the evolution of a primitive body it may be desirable to collect sample from lower depths created during embedding. Surface alteration on primitive bodies from space weathering has been shown to only alter materials on depth scales of nanometers [41], while changes resulting from impact of micrometeorites remain uncertain given the variability of impactors and poorly understood mixing processes that occur over time [42]. The ability to collect samples from specific depths could vastly improve our understanding of these processes. This could be possible through the further development of feed port covers designed to abrade away, preventing the collection of material above a given depth, or allowing for the collection of materials from specific depths. This method could be used to create a longer chronological picture of the sampled body by using

multiple penetrators, each with covers designed to abrade at different rates, resulting in a series of cores collected from different depths.

5.3 FUTURE WORK

Results from field testing demonstrate the feasibility of the use of penetrators for sample return, but further investigation into processes at work during the embedding will be required to complete a more quantitative assessment of the system. Shock wave propagation and the characteristics of the flow of sample material during collection are poorly understood, and will require extensive modeling followed by additional testing to parameterize what primitive bodies might be appropriate for this method of sample collection.

The geometry of the nose cone, whether the hybrid configuration in section 3.3 or the fully forward SRC in section 3.4, produces and annular contact surface from which wave propagate spherically at the material sound speed out from the initial impact point. The annular geometry also produces a wave that propagates inward, but how this wave effects material flowing through the system is unknown. Additionally, little is understood concerning the flow characteristics of materials in regimes that are beyond plastic deformation during the cataclastic flow that occurs during sampling. Smooth Particle Hydrocode would lend insight into the behavior of the material under sampling conditions. The original stratigraphy of the target area discussed in section 3.4 was largely preserved, but the impact velocity was only half of the sandstone shot in which uncertainties remain concerning how much information is lost during the repacking of the mineralogy. New thin sections of the sampled sandstone would provide more insight into this process, and is necessary for the identification of the orange ring. The results of the thin section analysis should be combined with SPH modeling for a clearer idea of processes occurring in the sample material during embedding.

Another variable that was not taken into consideration during testing was the macroporosity of the target material. Our understanding of asteroids in our solar system has expanded greatly over the last two decades, highlighted by the striking observation that when density values taken from collected meteorites were compared with the observed volume of primitive bodies assumed to have similar compositions, results suggested that many of these objects may contain nearly as much empty space as they do accreted material [40]. The effect of porosity on impact depth will need clarification before the selection of a potential sampling target can be made since this will have major implications for the acceleration profile of the penetrator, and as such pressures created during sampling.

Finally, a trade study should be conducted concerning the recovery of the sample by the spacecraft. Limitations during this phase of research dictated the focus on the proof-of-concept for the use of penetrators for sample collection, and did not allow for a full analysis of the spacecraft used to deploy the system. Recovery of the sample was initially conceived using up to 100 kilometers of tether, but this introduces multiple complications in the recovery of the SRC and may in fact not be practical. The self-ejection of the SRC demonstrated in section 3.4 points to multiple methods of retrieving the sample since an ejection velocity of 10 m/s on Earth would be more than enough to place the SRC on the surface away from the impact site on even the largest primitive bodies like Ceres and Vesta.

Chapter 6. CONCLUSION

Sample return missions offer a greater science yield when compared to missions that only employ in situ experiments or remote sensing observations, since they allow the application of more complicated technological and analytical methodologies in controlled terrestrial laboratories that are both repeatable and can be independently verified. Sampling methodologies applied over more than forty years have employed both manned and un-manned missions, with varying degrees of success. Manned missions to the Moon have provided the greatest return yields to date, but current technology limits our ability to place astronauts in environments that are too hazardous for the time scales necessary for adequate sample collection. Un-manned missions have demonstrated the ability for autonomous sample collection using soft-landing, touch-and-go, or no contact strategies, but at the cost of only returning a small fraction of surface materials that have experienced varying degrees of alteration from space weathering.

A new concept for sample return missions was investigated using planetary penetrators to collect subsurface materials at higher return yields than previous autonomous methods. By utilizing the momentum imparted by a passing spacecraft, penetrators could be deployed to collect samples from primitive bodies in the solar system, reaching depths of 1 to 2 meters. As the penetrator impacts the target, feed ports in the nose cone allow for a cataclastic flow of material to pass through the system for collection in the SRC. Pressures created during embedding eject the SRC from the impact site for collection which lowers the overall expense of the mission since significant changes to the spacecraft's velocity are not required.

A proof-of-concept study on the feasibility of using penetrators for sample return was conducted over a three year period. The study focused on three major goals: (1) the survivability of the SRC under subsonic and supersonic impact velocities (200-700 m/s); (2) the

successful collection of sample material during impact; (3) the self-ejection of the SRC for later collection and analysis. A key component in the design of the penetrators was the creation of energy absorbing materials from composite materials that could protect the SRC during embedding, as well as the design and fabrication of nose cones machined from materials harder than the target material.

Early field tests demonstrated the ability to penetrate more than a meter into a variety of materials, but the elastic response of the sample material resulted in stagnation regions which prevented samples from reaching the SRC. Further design evolutions resolved the stagnation problems, allowing for 1.6 meters of penetration into sandstone at ~630 m/s. The test revealed flaws in the modeling of the target material behavior that directly resulted in the failure of the SRC to eject. A final evolution that moved the SRC full forward in the assembly was executed, resulting in the successful collection of target material and the self-ejection of the SRC at an impact velocity of about 300 m/s. Following the testing, the samples were examined to assess the viability of the collected materials.

The potential for metamorphic effects on the sampled mineralogy was assessed by a precursory examination thin sections made from the impacted sandstone. While no major alterations to the mineralogy were observed, the impact created an annular discontinuity; difficulties in maintaining the cohesion of the sandstone during thin sectioning prevented the quantitative identification of the discontinuity, with the most likely hypothesis suggesting it was the result of oxidized steel abraded and entrained during embedding. More positive results were found upon examining the 300 m/s impact when the SRC was opened to reveal no metamorphic effects, and the preservation of the stratigraphy observed at the impact site.

The use of planetary penetrators for sample return missions has been demonstrated at a proof-of-concept level, but much work remains to be done. A clearer understanding of the dynamic process occurring during impact will require the implementation of SPH modeling to assess the characteristics of cataclastic flow created during sampling. Thin sectioning of the impacted sandstone will have to be redone in order to discover the composition of the annular discontinuity necessary to identify the mechanisms that created it. Finally a trade study assessing alternate recovery methods must be done since the viability of the use of long tethers is now in question.

As humanity moves into its next phase of space exploration, the need for sample return has never been greater. These missions will provide critical information needed for both purely commercial development as well as the identification of potential in-situ resources we will need to expand our presence out into the solar system. The use of planetary penetrators could reduce the expense of these missions while increasing the return yield, providing us with not only a map to the stars, but with the understanding of how we came to be as we unlock the mysteries hidden in the depth of our neighbors.

BIBLIOGRAPHY

[1] National Research Council, Committee on the Planetary Science Decadal Survey. 2011. "Vision and Voyages for Planetary Science in the Decade 2013-2022". National Academy of Sciences, Washington DC. www.nap.edu.

[2] Mueller, R.P., P.J. van Susante. 2012. "A Review of Extra-Terrestrial Mining Robot Concepts". *Earth and Space 2012: Engineering, Science, Construction, and Operations in Challenging Environment, Symposium 2: Exploration and Utilization of Extraterrestrial Bodies.* ASCE. doi: 10.1061/9780784412190.034

[3] Sandford, S. 2014. "An Overview of the OSIRIS-REX Asteroid Sample Return Mission". SSERVI Exploration Science Forum. NASA Ames Research Center, Bld. 152. Moffet Field, CA. 21 July 2014. Invited speaker.

[4] Drake, M.J., K. Righter. 2002. "Determining the composition of the Earth". Nature, Vol. 416, 39-44.

[5] Brucato, J. R., A. Rotundi, E. Mazzota Epifani. 2009. "Sample Return Missions from Minor Bodies: Achievements, Future Plan and Observational Support". Earth Moon Planet, 105, 273-282. doi: 10.1007/s11038-009-9336-5.

[6] Shevchenko, V.G., R.A. Mohamed. 2005. "Spacecraft Exploration of Asteroids". Solar System Research, Vol. 39, No. 1, 2005, 73-81.

[7] Chapman, C.R.. 1996. "S-type asteroids, ordinary chondrites, and space weathering: The evidence from Galileo's fly-bys of Gaspra and Ida". Meteorites & Planetary Science 31, 699-725.

[8] Brunetto, R.. 2009. "Space Weathering of Small Solar System Bodies". Earth Moon Planet, 105:249-255. doi: 10.1007/s1038-009-9340-9.

[9] Neal, C. R.. 2009. "The Moon 35 years after Apollo: What's left to learn?". Chemie der Erde, 69, 3-43. doi:10.1016/j.chemr.2008.07.002.

[10] Gibney, Elizabeth. 2014. "Rosetta probe makes history by landing on comet". Nature News. Nature Publishing Group. doi:10.1038/nature.2014.16340.

[11] ESA. 2014. Image: Rosetta at Comet. ESA/ATG Medialab. http://www.esa.int/var/esa/storage/images/esa_multimedia/images/2014/11/rosetta_at_comet_landscape/15031338-1-eng-GB/Rosetta_at_Comet_landscape.jpg

[12] Malik, T. 2015. “It’s Alive! Comet Lander Philae Phones Home After Months of Silence”. Space.com. http://www.space.com/29661-philae-comet-lander-wakes-up.html

[13] NASA. nd. “OSIRIS-Rex Exploring Our Past, Securing Our Future Through Pioneering Asteroid Science”. Goddard Space Flight Center, Greenbelt, Md.. http://www.nasa.gov/centers/goddard/pdf/552572main_OSIRIS_REx_Factsheet.pdf

[14] Neal-Jones, N., B. Steigerwald, R. Garner Ed. 2013. Image: OSIRIS-Rex, TAGSAM. NASA Goddard Space Flight Center, Greenbelt, Md.. http://www.nasa.gov/topics/solarsystem/features/osiris-rex-security.html

[15] Marín, D.. 2014. “Manda tu nombre al asteroid Bennu”. Eureka, 18 Jan., 2014. Images credited to NASA. http://danielmarin.naukas.com/2014/01/18/manda-tu-nombre-al-asteroide-bennu.

[16] Yeomans, D.. 2005. “Hayabusa’s Contributions Toward Understanding the Earth’s Neighborhood”. NASA, Jet Propulsion Laboratory, California Institute of Technology, Pasadena, CA. http://neo.jpl.nasa.gov/missions/hayabusa.html.

[17] Todd, N. S.. 2015. “Hayabusa Asteroid Itokawa Samples”. NASA, Curation, Hayabusa. http://curator.jsc.nasa.gov/hayabusa.

[18] JAXA. 2003. “Asteroid Explorer Hayabusa2”. Satellites and Spacecraft. Japan Aerospace Exploration Agency. http://global.jaxa.jp/projects/sat/hayabusa2/index.html.

[19] Meyer, A.. 2009. “Genesis Search for Origins: Mission History”. NASA, Jet Propulsion Laboratory, California Institute of Technology, Pasadena, CA. http://genesismission.jpl.nasa.gov/gm2/mission/history.htm.

[20] Whalen, A.. 2009. “Stardust NASA’s Comet Sample Return Mission”. NASA, Jet Propulsion Laboratory, California Institute of Technology, Pasadena, CA. http://stardust.jpl.nasa.gov/home/index.html.

[21] Lorenz, R.D.. 2011. “Planetary penetrators: Their origins, history and future”. Advances in Space Research, 48, 403-431. doi: 10.1016/j.asr.2011.03.033.

[22] Surkov, Y.A., R.S. Kremnev. 1998. “Mars-96 mission: Mars exploration with the use of penetrators”. Planetary Space Science, Vol. 46, No. 11/12, pp.1689-1696.

[23] JPL Special Review Board. 2000. “Report on the Loss of the Mars Polar Lander and Seep Space 2 Missions”. Jet Propulsion Laboratory, California Institute of Technology. JPL D-18709.

[24] Lorenz, R.D., J.E. Moersch, J. A. Stone, A. R. Morgan Jr, S.E. Smrekar. 2000. "Penetration tests on the DS-2 Mars microprobes: penetration depth and impact velocity". Planetary and Space Science 48, 419-436.

[25] Nakajima, T., M. Hinada, H. Mizutani, H. Saitoh, J. Kawaguchi, A. Fujimura. 1996. "LUNAR PENETRATOR PROGRAM: LUNAR-A". Acta Astronautica, Vol. 39, No. 1-4, pp. 111-119.

[26] Mizutani, H.. 1995. "Lunar Interior Exploration by Japanese Lunar Penetrator Mission, LUNAR-A". Journal of Physics of the Earth, 43, 657-670.

[27] Institute of Space and Astronautical Science (ISAS). 2008. "LUNAR-A". Japan Aerospace Exploration Agency. http://www.isas.jaxa.jp/e/enterp/missions/lunar-a/.

[28] Asphaug, E. 2009. "Growth and Evolution of Asteroids". The Annual Review of Earth and Planetary Sciences, 39:413-48. doi: 10.1146/annurev.earth.36.031207.1274214.

[29] Yano, H., T. Kubota, H. Miyamoto, T. Okada, D. Scheeres, Y. Takagi, K. Yoshida, M. Abe, S. Abe, O. Barnouin-Jha, A. Fujiwara, S. Hasegawa, t. Hashimoto, M. Ishiguro, M. Kato, J. Kawaguchi, T. Mukai, J. Saito, S. Sasaki, M. Yoshikawa. 2006. "Touchdown of the Hayabusa Spacecraft at the Muses Sea on Itokawa". *Science*, New Series, Vol. 312, No. 5778, pp. 1350-1353.

[30] Winglee, R. M., C. Truitt, R. Hoyt. 2013. "Sample Return Systems for Extreme Environments". Final Report for NNX12AR02G. NASA. http://www.nasa.gov/sites/default/files/files/Winglee_2012_PhI_SampleReturnExtreme.pdf.

[31] Witold, S., J. Desmons, D.J. Fettes, B. Harte, F.P. Sassi, R. Schmid. 2003. "A systematic nomenclature for metamorphic rocks: 2. Types, grade and facies of metamorphism." *Recommendations by the IUGS Subcommission on the Systematics of Metamorphic Rocks.* Web version. http://www.bgs.ac.uk/scmr/docs/papers/paper_2.pdf.

[32] Winter, J.D.. 2001. *An Introduction to Igneous and Metamorphic Petrology*. Upper Saddle River: Prentice-Hall, Inc.. Print.

[33] Tindle, Andy. nd. "Reference Cards for Geologists, Metamorphic Facies." http://www.open.ac.uk/earth-research/tindle/AGT/AGT_Home_2010/Ref_Cards.html.

[34] French, B.M.. 1998. *Traces of Catastrophe: A Handbook of Shock-Metamorphic Effects in Terrestrial Meteorite Impact Structures.* LPI Contribution No. 954, Lunar and Planetary Institute, Houston.

[35] Young, C. W.. 1967. "The Development of Empirical Equations for Predicting Depth of an Earth-Penetrating Projectile". Sandia Laboratory, Albuquerque. SC-DR-67-60. doi: 10.2172/4337362.

[36] National Research Council. 2005. *Effects of Nuclear Earth-penetrator and Other Weapons*. The National Academies Press. Washington, D.C. Web. http://www.nap.edu/openbook.php?record_id=11282.

[37] Creely, S., E. R. Force. 2007. "Type Region of the Ione Formation (Eocene), Central California: Stratigraphy, Paleogeography, and Relation to Auriferous Gravels". Open-File Report 2006-1378. U.S. Department of the Interior. U.S. Geologic Survey. http://pubs.usgs.gov/of/2006/1378/.

[38] Dawson, T. E. 2009. "Preliminary Geologic Map of the Lodi 30' x 60' Quadrangle, California". California Department of Conservation, California Geologic Survey. ftp://ftp.consrv.ca.gov/pub/dmg/rgmp/Prelim_geo_pdf/Lodi_100K_prelim.pdf.

[39] Bartow, J. A.. 1992. "Contact relations of the Ione and Valley Springs Formations in the east-central Great Valley, California". Open-File Report 92-588. U.S. Department of the Interior, U.S. Geologic Survey. http://pubs.usgs.gov/of/1992/0588/report.pdf.

[40] Consolmagno, G., D. T. Britt, K. Housen, D. Yeomans. 2003. "Asteroid Density, Porosity, and Structure". Web. http://www.lpi.usra.edu/books/AsteroidsIII/pdf/3022.pdf.

[41] Noguchi, T., T. Nakamura, M. Kimura, M. E. Zolensky, M. Tanaka, T. Hashimoto, M. Konno, A. Nakato, T. Ogami, A. Fujimura, M. Abe, T. Yada, T. Mukai, M. Ueno, K. Shirai, Y. Ishibashi, R. Okazaki. 2011. "Incipient Space Weathering Observed on the Surface of Itokawa Dust Particles". Science. Vol. 333. http://science.sciencemagazine.org/.

[42] Pieters, C. M., E. Ammannito, D. T. Blewett, B. W. Denevi, M. C. De Sanctis, M. J. Gaffey, L. Le Corre, J. Y. Li, S. Marchi, T. B. McCord, L. A. McFadden, D. W. Mittlefehldt, A. nathues, E. Palmer, V. Reddy, C. A. Raymond, C. T. Russel. 2012. "Distinctive space weathering on Vesta from regolith mixing processes". Nature, Vol 491. doi: 10.1038/nature11534.